FERMILAB-PUB-20-104

Prepared for submission to JINST

Design and performance of an in-vacuum, magnetic field mapping system for the Muon g-2 experiment

S. Corrodi,[a] **P. De Lurgio,**[a] **D. Flay,**[b] **J. Grange,**[a] **R. Hong,**[a,1] **D. Kawall,**[b] **M. Oberling,**[a] **S. Ramachandran**[a] **and P. Winter**[a,2]

[a] *Argonne National Laboratory, High Energy Physics Division, 9700 S Cass Ave, Lemont, IL 60439, USA*
[b] *University of Massachusetts Amherst, Amherst, MA 01003*

E-mail: winterp@anl.gov

Abstract: The E989 Muon $g-2$ experiment at Fermilab aims to measure the anomalous magnetic moment, a_μ, of the muon with a precision of 140 parts-per-billion. This requires a precise measurement of both the anomalous spin precession frequency, ω_a, of stored muons and the average magnetic field in terms of the equivalent, free proton Larmor frequency, ω_p. The measurement of ω_p with a total systematic uncertainty of 70 parts-per-billion involves a combination of various nuclear magnetic resonance (NMR) probes. There are 378 probes mounted in fixed locations that constantly monitor field drifts. A water-based, cylindrical calibration probe provides the calibration in terms of the free proton Larmor frequency. A crucial element for the multi-step measurement of ω_p is the regular mapping of the magnetic field over the muon storage region. The former E821 experiment at Brookhaven employed an in-vacuum field mapping system equipped with 17 NMR probes, which was developed by the University of Heidelberg. We have refurbished and upgraded this system with new probes and electronics. The upgrades include a new communication scheme incorporating time-division multiplexing to separate the important NMR reference clock from the data communication in order to reach the specifications for the accuracy and stability of the reference clock. The addition of 16-bit, 1 MSPS digitization of the NMR signals replaced the hardware-implemented zero-crossing counting of the E821 system. The digitized signals offer new capabilities in the NMR frequency analysis and its related systematic uncertainties. While the mechanical systems that move the field mapper inside the storage ring have been mostly refurbished from E821, the motion control system was completely replaced with a custom-built electronics centered around a commercial Galil motion controller. Both the field mapping NMR system and its motion control were successfully commissioned at Fermilab and have been in reliable operation during the first three data taking periods of the E989 experiment. This article will provide the details of the upgrades of the field mapper and its performance.

[1] Now at University of Kentucky
[2] Corresponding author.

Contents

1 Introduction

The Muon $g-2$ E989 experiment at Fermilab [1] will measure the muon anomalous magnetic moment, a_μ, with a precision of 140 parts-per-billion (ppb), a four-fold improvement over the former experimental results. This is motivated by the current discrepancy of $\sim 3.5\sigma$ between the former results [2] and the Standard Model predictions [3–6] which could be a sign of new physics.

The experimental principle is very similar to the E821 experiment at Brookhaven National Laboratory (BNL) using stored muons in a very homogeneous magnetic field B$\simeq$1.45 T. Muons at the magic momentum of $p = 3.094$ GeV/c are injected into the storage ring through an inflector magnet [7] that zeroes the main field in the injection channel. A subsequent fast magnetic kicker deflects the muons onto a stable orbit and electrostatic quadrupoles provide vertical focusing.

The determination of a_μ requires a precise measurement of both the anomalous spin precession frequency of the stored muons, ω_a, and the magnetic field of the storage ring in terms of the free proton Larmor frequency, ω_p. The measurement of ω_a is based on the time and energy spectrum of the decay positrons measured in 24 electromagnetic calorimeters made from PbF_2 Čerenkov crystals [8] in conjunction with many other systems like a laser calibration and in-vacuum straw tracker stations. The measurement of the magnetic field with a target systematic uncertainty of better than 70 ppb is achieved through the following: 1) Passive and active shimming to prepare a very uniform field, 2) constant monitoring of the storage field drift over time with 378 pulsed NMR probes mounted above and below the storage region, 3) frequent field mapping of the storage region with an in-vacuum, pulsed NMR system, and 4) the calibration referencing the measurements against the free-proton Larmor frequency with an accurate and precise water-based NMR probe.

The in-vacuum field mapping system, the so-called trolley, plays an essential role in measuring the magnetic field. Its main purpose is to map the magnetic field over the muon storage region of the 45-meter-long circumference of the storage ring. The trolley system was inherited from the experiment E821 at BNL [9]. The main components of the original system were:

- The trolley located inside the vacuum chambers consisted of a vacuum-sealed aluminum cylinder with 17 NMR probes, readout electronics, and auxiliary sensors. The system was centered around a Motorola MC68332 microcontroller unit with an integrated time processing unit that was used for processing of the NMR signals. An on-board communication module facilitated the serial communication with an external interface located outside the vacuum.

- The external interface provided the RS232 communication from a computer, the power, and the radio frequency (RF) signal for the NMR measurement via a single coaxial cable to the trolley. It also received the data from the trolley via RS232 and routed it to the computer.

- A drive system consisting of two cable drums operated by piezo-electric motors from Shinsei connected to the storage ring vacuum chambers in the experiment. Two cables, one a nylon line and the other a coaxial cable, were routed and connected to the trolley to pull it the full 360° around the storage ring in both directions.

- A garage mechanism that consisted of a trolley rail section in the vacuum chambers connected to a Shinsei motor via threaded rods. The mechanism was used to retract the trolley system from the muon storage region during muon injection.

- A controller for the motor motion for both the drive and garage operation which received the readbacks from various encoders and other sensors. An integrated Siemens 80C535 micro-controller unit was programmed to control the three motors so that the trolley could be moved around the entire muon storage region to map the magnetic field.

Many elements in the E821 trolley and motion control systems were outdated or end-of-life components and required replacement. The five key upgrades for the E989 trolley system are:

1. The obsolete Motorola controller inside the E821 trolley has been replaced with a low-power SmartFusion System-on-Chip (SoC) that facilitates the control of the NMR measurement sequences, the data readout, and the communication with the interface outside the vacuum.

2. The single coaxial cable connection requires multiplexing of various signals (power, a 61.74 MHz precise reference clock signal, and the data communication). To separate the reference clock and data communication, time-division multiplexing (TDM) has been implemented through the addition of two RF switches on either end of the cable.

3. The NMR free induction decay (FID) signal is fully digitized on-board with a 16-bit, 1 MSPS analog-to-digital converter (ADC). The digitization replaces a hardware-implemented zero-crossing-counting in the E821 system.

4. Improvements in the azimuthal position determination of the trolley come from a new barcode reader that records regular and irregular marks on the bottom of the vacuum chambers.

5. The NMR probes were replaced with new ones built by the University of Washington based on the same design used for the 378 fixed probes.

The mechanism to park the trolley prior to muon injection and the cable pulling drums were refurbished. Both systems are operated by piezo-electric motors that can operate in the high magnetic field. The E821 motion controller unit with the obsolete Siemens 80C535 micro-controller has been replaced by a commercial Galil DMC-4183[1] motion controller combined with custom built electronics interfacing with the motors, tension sensors, rotary encoders, and other sensors. Both the new trolley NMR electronics and motion control system were successfully commissioned and have been operating well during the first data taking periods.

The upgrade of the system was constrained by several system requirements. The most important of these requirements were to i) exclude usage of ferromagnetic materials and minimize the magnetic footprint; ii) keep the total power consumption of the on-board electronics to less than 1 W due to limited heat dissipation in the vacuum; and iii) maintain the single coaxial cable to provide power, communication, and the precision RF signal. Additional requirements included the physical space limitation inside the trolley shell, the goal of reusing parts where possible for cost efficiency, and to provide a full remote operation of the trolley from the control room.

This article describes the details of the field mapping system upgrades for the E989 Muon $g-2$ experiment at Fermilab. Section 2 focuses on the trolley with its external interface. Section 2.2 will give an overview of the general design considerations and requirements for the system. The air-side components will be described in Sections 2.3 and 2.4 and Section 2.5 will focus on the vacuum-side NMR and barcode reader electronics inside the trolley. Section 3 details the mechanical system upgrades with the drive and garage in Section 3.2 and the new Galil motion control in Section 3.3. Section 4 summarizes the performance of the new systems.

2 In-vacuum field mapping NMR and barcode reading system

2.1 Overview of the system

The field mapping system is schematically shown in Figure 1. It comprises air-side components outside of the storage ring vacuum chambers and the vacuum-side field-mapping trolley. A Meridian Precision GPS TimeBase[2] module from Endrun Technologies provides the inter-range instrumentation group code B (IRIG-B) timestamps and disciplines a Stanford Research Systems (SRS) rubidium clock (FS725[3]), which delivers a precision 10 MHz clock to both the trolley interface and a SRS SG380 signal generator[4]. The SG380 unit generates a precise 61.74 MHz RF signal that is routed via the trolley interface to the trolley for the NMR measurement. A Linux PC controls and monitors the NMR measurement via the trolley interface module, which facilitates the control and communication with the vacuum-side trolley and multiplexes all signals onto a single coaxial cable.

2.2 Design requirements for the NMR system

The main purpose of the NMR field mapping trolley is to provide detailed field maps over the entire muon storage region so that the magnetic field averaged over the entire azimuth of the storage ring can be determined with a precision of better than 30 ppb. The upgrades to the existing E821 trolley

[1] http://www.galilmc.com/motion-controllers/multi-axis/dmc-41x3
[2] https://endruntechnologies.com/pdf/MeridianGpsTimeBase.pdf
[3] https://www.thinksrs.com/products/fs725.html
[4] https://www.thinksrs.com/products/sg380.html

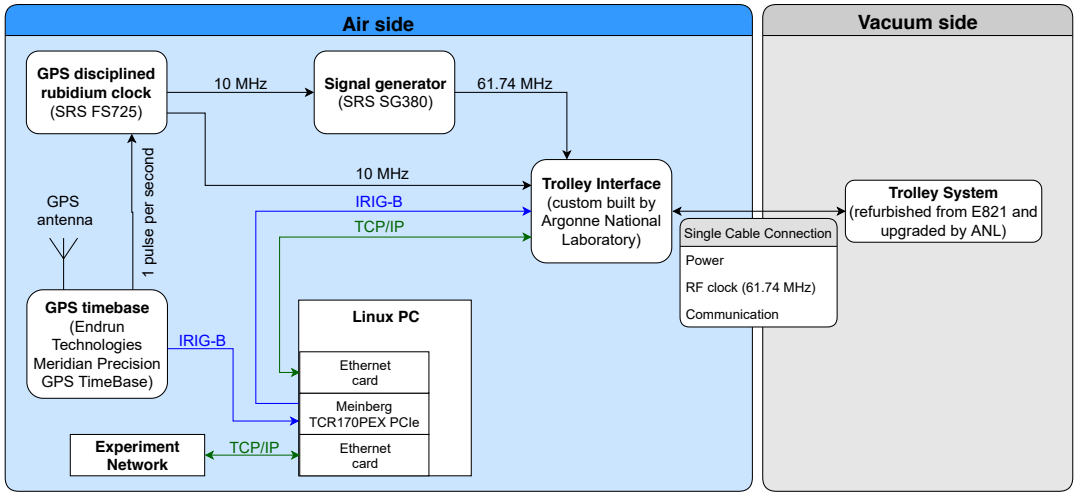

Figure 1: Schematic diagram of the main trolley components. More detailed diagrams of the custom built interface, single cable connection, and trolley are shown in later sections.

had to comply with the following requirements, which were derived from the primary precision goals during the development of the technical design report [1]:

- The single-shot precision of each probe has to be better than 20 ppb in a homogeneous field region in order to determine the averaged field to better than 30 ppb precision. This requirement was derived from simulations and data from the E821 experiment assuming at least 6000 measurements along the azimuthal for each probe as well as improved position determination from the new barcode reader (see below).

- The precision requirements for the NMR measurement necessitates study of the dependence of the extracted NMR frequency on effects like baseline shifts, noise, or field gradients with a precision of a few ppb. This requires digitization of the FID signal after it is mixed down from ~61.79 MHz to ~50 kHz. To be significantly above the Nyquist frequency, the digitizer must have a minimum of a few 100 kSPS.

- The overall precision goal for the averaged field requires a precise knowledge of the trolley position during each measurement to perform a correct averaging of the azimuthal field distribution. Based on the expected improved field homogeneity in E989 due to better shimming and sample field distributions from E821, simulations showed that the azimuthal position of each measurement should have a precision of better than 5 mm.

- Because the system operates in vacuum, heat dissipation is limited by radiation from the shell, which leads to a temperature change of the NMR probes and with it the NMR frequency. In E821, the probes' temperatures changed by about 1.5 K during the measurement period. To keep the temperature rise inside the trolley below that observed in E821, the maximum average power for the trolley system (including the new barcode reader) was 1 W.

- The operation in vacuum had to comply with the externally provided maximum vacuum load of less than $5 \cdot 10^{-5}$ Torr l/s for any system introduced to the vacuum region.
- As the trolley maps the field, it also provides calibrations for each of the 378 stationary fixed probes. However, the trolley materials slightly distort the field around the trolley, requiring the fixed probe analysis to veto a window when the trolley is nearby. Minimization of the trolley magnetic footprint reduces the required veto window and is beneficial for this fixed probe calibration. Each new component introduced during the upgrades was required to be as non-magnetic as reasonably possible. The maximum magnetic distortion of the trolley in E821 was ~24 ppm [10] and the requirement for the new system was to be less than that.
- The field mapping with the trolley is incompatible with muon injection. To minimize the interruption of the muon beam, the trolley should drive at least as fast as in E821 (about 1 cm/s). A faster speed of the trolley also requires a faster NMR repetition rate for each probe in order to achieve the same amount of measurements. For our probes, the maximum repetition rate, limited by the relaxation time of petroleum jelly, is about 2 Hz. To achieve the minimum of 6000 measurements, the trolley speed has an upper limit of 1.5 cm/s. The trolley speed requirement was therefore between 1 and 1.5 cm/s.

Besides the above listed specific requirements, efforts were taken to reuse existing parts where possible to maximize cost efficiency.

2.3 Air-side GPS timebase, RF, and IRIG-B sources

Three pieces of hardware in Figure 1 are relevant for the clock, RF, and timestamp distribution: i) the Meridian Precision GPS (GPS) TimeBase unit, ii) the SRS FS725 rubidium clock, and iii) the SRS SG388 signal generator. The Meridian Precision GPS TimeBase unit from Endrun Technologies is connected to a GPS antenna and sends a precise 1 pulse-per-second (pps) to the SRS FS725 rubidium frequency standard to stabilize its long-term drift. The Meridian Precision GPS TimeBase also acts as the distribution source for the IRIG-B timestamps via a daisy-chain across the experiment. Each computer that needs to be synchronized is equipped with a TCR170PEX PCIe interface card[5] from Meinberg. At the end of the chain is the trolley interface, which provides 50 Ω termination and decodes the IRIG-B signal for the trolley (see Section 2.4).

The SRS FS725 module has an internal rubidium clock that stabilizes all critical systems in the entire experiment via a distributed 10 MHz reference clock. For the trolley system, two modules receive this 10 MHz signal: the SRS SG380 signal generator and the trolley interface. The rubidium oscillator of the FS725 has an accuracy of $\pm 5 \times 10^{-11}$ with a yearly aging of less than 5×10^{-10}, which is even further decreased through the GPS synchronization via the 1 pps signal. This accuracy surpasses the requirements for the main clock of the Muon $g-2$ system resulting in a negligible systematic uncertainty compared to the overall precision goal on a_μ.

One of the 10 MHz signals from the FS725 unit is sent to the trolley interface where it is phase locked with the received IRIG-B signal for decoding of the timestamp. A second 10 MHz signal stabilizes the SRS SG380 signal generator, which is a critical element for the NMR measurement.

[5] https://www.meinberg-usa.com/products/pci-and-pcie-slot-cards/pci-express-irig-time-code-receiver-generator.htm

The module provides a very precise and stable 61.74 MHz RF reference clock to the trolley interface where it is multiplexed onto the single coaxial cable connected to the trolley. The purpose of this RF signal is two-fold. It is used to rotate the spins in the NMR sample by $\pi/2$ (perpendicular to the magnetic field). The second purpose of the RF signal is to mix down the free induction decay signal from ~61.79 MHz to ~50 kHz. The storage field is 1.45 T, the NMR frequency of protons in the petroleum jelly is close to 61.79 MHz, about 50 kHz above the RF reference clock. The requirement for the reference signal was an accuracy and stability of better than 10^{-9}, which is achieved through the specifications of the FS725 unit. As will be described in Section 2.5, the mixed down FID signal is digitized inside the trolley. The high precision of the 61.74 MHz RF signal used to generate the mixed down frequency of ~50 kHz relaxes the requirements on the relative precision of the measured FID frequency by 10^3.

2.4 Air-side trolley interface

The trolley interface unit is a custom 3U 19" rack-mount module shown in Figures 2a and 2b. The interface contains three major sections: a power supply, a custom-built carrier board, and the central MicroZed controller board. More details of the interface and its important components are shown in the block diagram in Figure 3. The system power is provided by a 120 V AC to DC linear regulated power supply (Acopian 51515T9AM) that generates −15 V, 15 V, and 5 V. The main MicroZed controller, the single cable communication (SCC), and the important elements of the custom-built carrier board will be described in Sections 2.4.1 to 2.4.4. The details of the control software and firmware implemented on the MicroZed are given in Section 2.6.

(a) (b)

Figure 2: (a) Front and back view of the trolley interface module. (b) Top view of the trolley interface with its cover removed showing the main components of the MicroZed board (red PCB) sitting on top of the custom built career board (green PCB) and the Acopian power supply (top).

2.4.1 MicroZed and single cable connection

The central control in the interface is provided through the Avnet MicroZed System-on-Module[6], which contains a Xilinx Zynq-7000 programmable system on chip (SoC) with integrated field

[6] http://zedboard.org/product/microzed

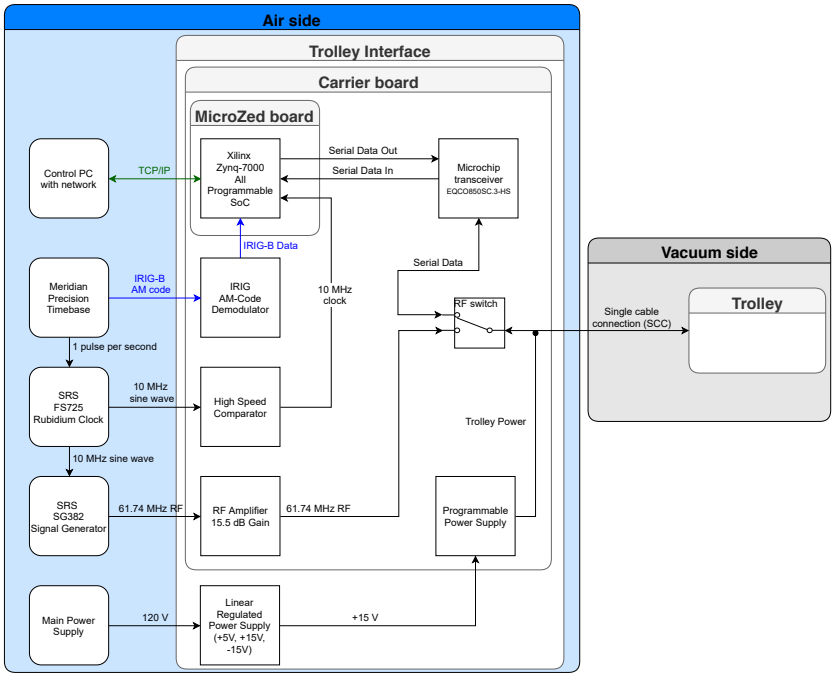

Figure 3: Schematic diagram of the trolley interface that controls and communicates with the trolley NMR enclosure inside the vacuum.

programmable gate arrays (FPGA). The control PC communicates with the MicroZed over a Gigabit Ethernet connection via TCP/IP and reads from and writes into registers that are subsequently handled by the ARM processor in the MicroZed. Firmware running on the Zynq FPGA uses these register values and executes the control of the trolley via the single cable communication (SCC).

The MicroZed is integrated onto a custom-built carrier board that incorporates the remaining elements needed to communicate with the trolley and control the NMR sequence and other sensors on-board of the trolley. The main subsections of this carrier board are the IRIG-B interface, an RF amplifier, a coaxial-driver, an RF switch, and a programmable power supply. The carrier board is equipped with a flash memory to facilitate trolley firmware updates over the SCC.

A major design change of the new trolley interface compared to the former E821 system is the modified control and communication scheme between the interface and the trolley. The modification was necessary due to the addition of NMR signal digitization in the trolley electronics (see details in Section 2.5.1), which led to a huge increase in data volume and rates. The communication in the E821 system was facilitated by a MAX232 dual driver/receiver using RS232 communication via TIA/EIA-232-F voltage levels. This chip was limited by a 15 kB/s maximum transmission rate. An estimate of the required minimum bandwidth for the new NMR digitization was based on the basic assumptions that a 16-bit ADC would digitize all 17 probes every second, with each being sampled for 5 ms at 1 MSPS. This led to a minimum data rate of about 200 kB/s if the data were sent from the trolley to the interface simultaneously to the data taking. The viability of modifying the E821 communication hardware to support the required bandwidth was tested, but an upper limit of 25 kB/s was found, an order of magnitude below the requirement. Alternative on-board storage,

allowing for delayed transfer at lower rates, was dismissed due to power consumption of available memory chips.

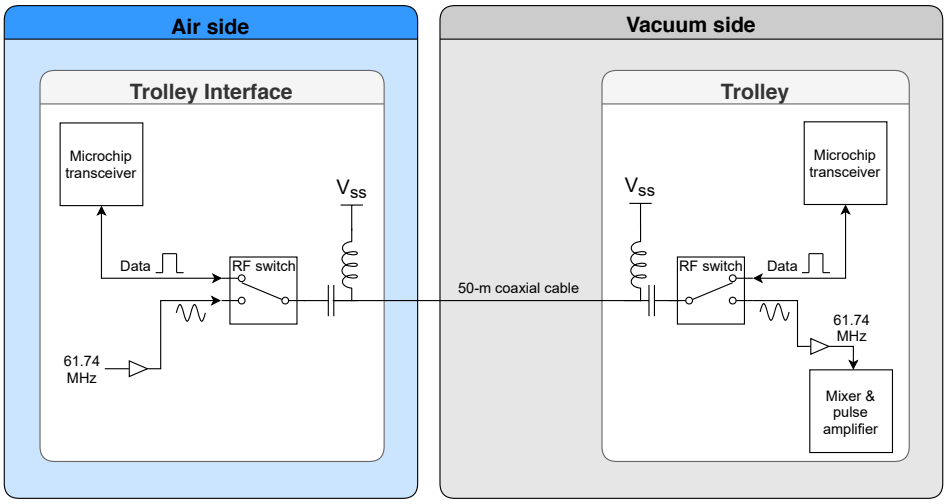

Figure 4: Schematic diagram of the new SCC scheme between the trolley interface and the trolley using time division multiplexing for the 61.74 MHz RF signal and the data communication.

A new scheme for the SCC (shown in Fig. 4) was developed, which replaced the former communication module inside the E821 trolley. The serial driver was replaced with a single-coax, full-duplex transceiver (EQCO850SC.3-HS) from Microchip that can maintain typical transmission rates of 500 Mbits/s over a 50 m long RG58 cable. Since the amount of data sent from the interface is small compared to the trolley's data payload, the chip is only operated as a half-duplex interface. The E821 experiment employed a ~50 m long Suhner G_G2232_D cable, which exhibited losses of about 17.5 dB/100 ft at a frequency of 62 MHz. To improve the cable quality for the higher data transmission in the new system, this cable was replaced with a non-magnetic, 50-m long, coaxial cable from Koaxis (type FF086), which has losses of 4 dB/100 ft at 62 MHz. A short section of the communication path inside the drive drum is facilitated by a smaller diameter, 5 m-long Koaxis cable (type FF047) (see also Section 3.2.1). Bench tests with a prototype design verified the achievable data rates significantly surpassed the minimum data rate requirement. However, extensive measurements of the phase noise described in Section 4.1.2 revealed that the first design with the new transceivers and multiplexing of all signals in parallel did not meet the precision requirements for the 61.74 MHz signal. The design was modified to implement time-division multiplexing (TDM) for the NMR RF clock and the data signals of the transceiver. This was accomplished by adding a high-isolation, single pole double throw (SPDT) switch (AD HMC349AMS8G) on both ends of the coaxial cable. The switch timing is controlled on the interface side by the Zynq (see also Section 2.6) through a Texas Instrument (TI) low-voltage differential signaling (LVDS) to low-voltage transistor–transistor logic (TTL) converter (DS90LT012A), which was chosen for its true differential logic to implement a break between the analog and digital ground. After implementation of TDM for separation of the RF signal from the data communication, the phase noise level for the crucial 61.74 MHz RF signal met the requirements (see Section 4.1.2).

2.4.2 Programmable trolley power supply

The carrier board on the interface includes a custom programmable linear power supply that is inductively isolated from the trolley coax to maintain the 50 Ω characteristic impedance required by the communication interface. This power supply circuit was added to the design for several reasons. First, the RF switches used on the SCC experience voltage transients during power-up. This is exacerbated by the significant amount of capacitance on the trolley, which increases the potential to expose the sensitive AC coupled RF input to the full supply voltage prior to the device being powered. Using a power supply that could be ramped slowly became a desirable option to limit this risk. In addition, the current varies significantly while conducting measurements and a significant voltage drop can occur on the cable due to the resistance of the long coaxial cable. The programmable output makes it possible to keep the average voltage for the trolley as low as possible to minimize the heat dissipation while providing enough overhead for stable measurements.

The trolley power supply utilizes a linear regulator (LT3089) with a single resistor to set the output voltage. It has a precise, 50 μA current source that develops a voltage in the range of 0 to 34.5 V via a single resistor between the regulator's SET and ground pins. In the trolley interface, the SET pin is connected to a pair of digitally controlled potentiometers (AD5282) in parallel with 150 kΩ resistors to give an output voltage range from 0 to 8.5 V on the LT3089. For a true 0 V output, a metal–oxide–semiconductor field-effect transistor (MOSFET) (DMG6968U) is connected to the output line of the LT3089 to short any small leakage current. The same circuitry is also used as part of the cable disconnection protection described in Section 2.6. A second DMG6968U between the SET pin and ground eliminates a small offset voltage from the digital potentiometer (POT).

2.4.3 IRIG-B decoding and clock receiver

In order to add precise timestamps to the trolley data for synchronization with other systems in the Muon $g-2$ experiment, the trolley interface receives IRIG-B signals and a very precise 10 MHz clock from the external Meridian and SRS FS725 modules, respectively. The IRIG-B decoder inside the trolley interface contains two main circuit blocks: a 10 MHz RF clock receiver and a IRIG-B demodulator. The 10 MHz receiver is transformer isolated and has an input impedance of 50 Ω at 10 MHz. The 10 MHz RF sinusoid is buffered by a rail-to-rail operational amplifier (TI OPA365) and then converted by a high speed comparator (LMH7220) into a precision LVDS clock. The 1 kHz IRIG-B amplitude-modulated signal is isolated with an audio transformer and sent to the demodulator circuit, which has an input impedance of 50 Ω. The output of the transformer is buffered by an op-amp (OPA365) and received by a pair of comparators (LMH7220). One comparator provides a 1 kHz demodulation clock and the other provides the IRIG-B data. A low jitter, 20 MHz oscillator (FXO-LC726R-200) on the carrier board provides an additional clock source in case the external 10 MHz clock input is lost. The circuitry also includes a precision voltage reference (REF5040) for setting the comparator voltage thresholds.

2.4.4 RF amplification

An important section on the carrier board is the RF amplification stage for the 61.74 MHz signal from the SRS SG382 precision RF source. The SG382 is capable of outputting 16 dBm maximum, but to reduce distortion and phase noise, its nominal output is typically set to 13 dBm for the

measurement. As described in Section 2.5.4, the generation of the $\pi/2$ pulse through the on-board RF amplifier of the trolley requires a 13 dBm RF signal at the trolley. The loss in the RF switches, the 50 m, and 5 m coax cables is about 15 dB at 62 MHz. Compensation of this loss is achieved with two high-voltage, current-feedback op-amps (TI THS3091). They are configured in parallel with output resistors and provide current sharing to achieve the required output power. In addition to the RF output for the SCC, the output of the THS3091 op-amps is used to generate a pair of clock signals. One is an NMR RF clock generated by a comparator (TI LMH7220) with LVDS output. This comparator has a threshold around the DC level of the input. A second comparator triggers with a threshold set to 66% of the peak voltage of the RF signal. The ratio of the 34% to 50% duty cycle signals provides a measure of the RF output power as described in Section 2.6.

2.4.5 Monitoring ADC

To monitor the output voltage and current sent to the trolley via the regulated power supply, the carrier board includes a 16-Bit, 1-MSPS, dual ADC (TI ADS8363) that is read out over a serial peripheral interface (SPI) bus. This monitoring ADC has either 8 pseudo- or 4 fully-differential input channels. In the trolley interface, 7 of the 8 pseudo-differential channels were used. The ADC monitors the trolley voltage through a resistor divider that is located after a 500 mA fuse, which serves as a fail-safe backup for the adjustable current limiter provided by the LT3089 linear regulator. In addition to the output voltage monitoring, the LT3089 regulator provides the ability to measure its output current and device temperature, which are monitored with the ADS8363. The same ADC also records the three voltages ($\pm$15 V and 5 V) from the Acopian power supply and a 3.3 V source generated on the carrier board with a LT3089 linear regulator.

2.5 Vacuum-side NMR and barcode electronics

The trolley system operates in the storage ring vacuum on the downstream end of the single coaxial cable (see Figure 4). Figure 5 shows the trolley enclosure with the attached external barcode reader (see Section 2.5.7). The cable clamp that attaches to both the coaxial and nylon cables is not attached in this picture. The two cables are part of the drive mechanism (see Section 3.2.1), which enables the movement of the trolley. A detailed block diagram of the new E989 trolley system is shown in Figure 6. The trolley enclosure is home to several separate units. The NMR electronics and the RF amplifier enclosures form one unit with two separated compartments. The NMR electronics enclosure is equipped with three electronics boards: the NMR main board, the auxiliary board, and the slightly modified E821 A296 board. These three boards will be described in Sections 2.5.1 to 2.5.3. The RF amplifier enclosure houses the RF amplifier, which was reused from E821 (see Sec. 2.5.4). These NMR electronics connect to the NMR multiplexer, the NMR preamplifier, and the NMR probes as described in Sections 2.5.5 and 2.5.6. Mounted on the outside of the main trolley enclosure is the barcode reader board (see Sec. 2.5.7).

2.5.1 NMR main board

The new NMR main board's key elements are represented in the block diagram of Figure 6. To mirror the functionality of the trolley interface with respect to the SCC, it is equipped with the same RF switch and Microchip coax transceiver. A SmartFusion 2 SoC (SF2) from Microsemi[7]

[7] https://www.mouser.com/new/microsemi/microsemi-smartfusion2-fpga/

Figure 5: The assembled trolley with the barcode reader board. The cable clamp is not yet attached.

was chosen as the main controller due to its low power consumption and capability to provide all the necessary functionality through its integrated FPGA and ARM processor. A photo of the main board is shown in Figure 7. It is the end-point of the SCC and receives the configuration data, the 61.74 MHz RF, and power from the interface. Various clocks for timing controls and all power supply voltages for the trolley system and barcode reader are generated on the main board.

In order to achieve the NMR resolution, careful routing of three ground planes was performed. A trolley system ground (effective Earth ground) connects to the electronic enclosure and to external objects inside the trolley enclosure. All connectors are referenced to it except for the barcode feed-through pins and the external temperature sensor, which are electrically isolated from other grounds. These two circuits are connected to the signal ground, which is isolated through inductors from the system ground. The signal ground references all trolley digital electronics including the SF2 and the ADCs. All fast signals crossing the signal-system ground boundary are differential. These include the serial data from the transceiver and the NMR ADC input signals. Only a few single-ended signals cross this ground plane break, but they are either slow or switch outside of the NMR measurement period when noise is less of a concern. The third ground plane is a small area isolated from system ground via inductors and serves as the reference for a DC-DC charge pump (LTC3265E).

The incoming RF exhibits losses over the coaxial cable and needs some additional amplification to generate the ~5 W $\pi/2$ pulse. This amplification is implemented with a high speed op-amp (ADA4857-1), which is configured as a band-pass amplifier centered at 62 MHz with 5 dB of gain. The input to the single-ended op-amp is treated differentially with the RF signal as the positive input and ground as the negative. This reduces common mode noise from sources like the power supplies. The RF output is fed into an SMA cable that connects to the A296 board. Here, the RF is used to either produce the $\pi/2$ pulse or provide the precision clock reference for the NMR mixer (see Section 2.5.3). A tap of the op-amp output feeds into a pair of comparators for the monitoring of the RF power similar to the RF amplification in the trolley interface (see Section 2.4.4).

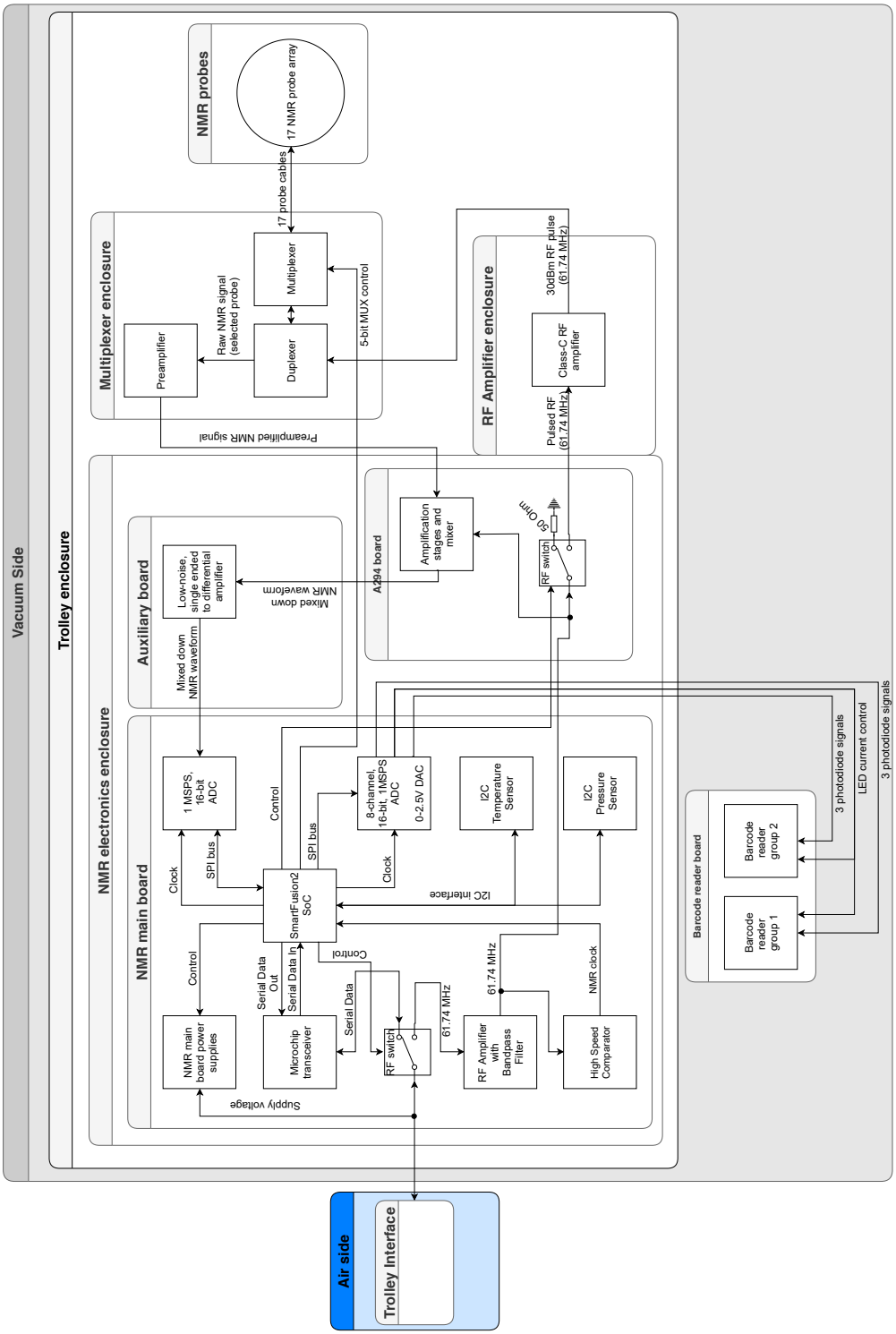

Figure 6: Schematic diagram of the trolley components.

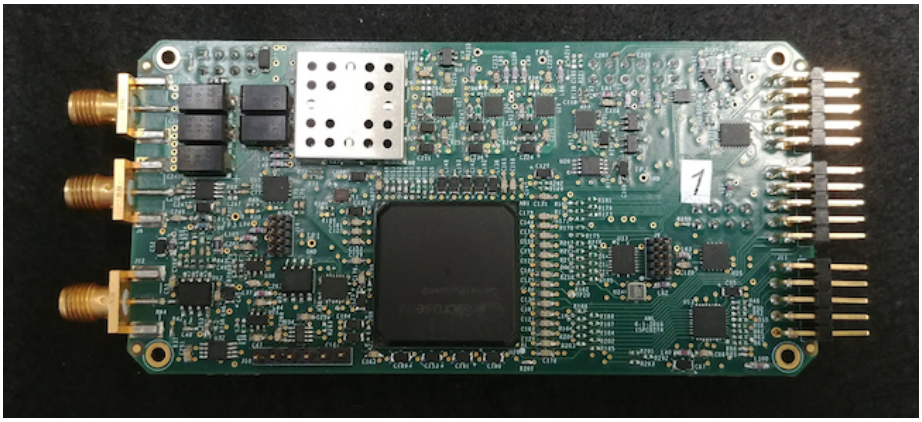

Figure 7: The assembled trolley main board with the SmartFusion 2 SoC chip.

At the center of the main board is the SF2 chip, which handles all readout control functionality. All interactions with the trolley are through command data packets sent from the trolley interface over the SCC. Each packet contains all possible trolley parameters, including measurement configurations and RF switch, measurement, and communication timing. Furthermore, the SF2 generates the clocks and provides the SPI interfaces for the two ADCs. The SF2 also controls the power supplies and the pressure and temperature sensors via an Inter-Integrated Circuit (I^2C) bus. Details of the NMR control sequences and other settings will be provided in Section 2.6.

The full digitization of each NMR waveform was a significant upgrade for the new system. The chosen ADC is a 16-bit, 1-MSPS, true differential input ADC with a serial interface (ADS8861). The conversion of the analog NMR signal from the A296 board to a differential signal was considered in the main board but dismissed to avoid noise pickup on this critical signal from the densely populated digital parts. The new auxiliary board offered physical separation from the main board to perform the conversion of the single-ended NMR signal into a differential signal without complete redesign of the A296 board. The ADC requires a reference voltage signal, which was implemented using a 4.096 V voltage reference (TI REF5040) and a pair of op-amps (OPA333 and THS428), which provide active filtering and low impedance for the ADC reference voltage input.

A second ADC on the main board is mainly used for the barcode signals and voltage monitoring. It is a dual 16-Bit, 1-MSPS simultaneous-sampling successive-approximation-register (SAR) ADC (ADS8363) with eight pseudo- or four fully-differential input channels grouped into two pairs. The ADC has a common SPI interface with two serial data outputs. The barcode (see Section 2.5.7) includes two groups of three LED-photodiode pairs with associated transimpedance readouts that are connected to six inputs of the ADC. The remaining two inputs are used for voltage monitoring as described below. The ADC has two digital-to-analog converters (DACs) which are used as the internal reference of the barcode ADC and the barcode LED current control, respectively.

A stable clock is derived inside the SF2 from the very precise 61.74 MHz RF reference signal received over the coaxial cable. This NMR clock is used for all timing of the NMR sequence and for the clocking of the ADC that is used to digitize the NMR waveform. For this ADC, the clock is further pre-scaled by 62. Since the nominal RF clock frequency is 61.74 MHz, the ADC clock is running at 0.996 MHz. A second, less precise clock is derived from an on-board 20 MHz oscillator

Table 1: List of generated trolley voltages with converter types and their application.

Voltage	Converter	Application(s)
−5 V	LTC3265	Front-end analog circuitry, band-pass RF amplifier
1.2 V	LT3042	SF2 core voltage, I/O bank, SF2 side of level translator ICs
3.3 V	LT3042	Most digital circuits, SF2 I/O banks
5 V	LT3042	NMR mux control, NMR front-end electronics, bandpass RF amplifier
10 V	LTC3265	Class-C RF amplifier

(7S-20.000MAHE-T) and handles less critical processes like the control of the general cycle timing or the clocking of the 8-channel ADC.

The operation of the trolley requires various supply voltages. The incoming supply voltage of about 6 V is decoupled from the SCC through a series of six 390 nH inductors to minimize the phase noise in the system while maintaining the characteristic impedance for reliable data communication. Large capacitor banks on the main and auxiliary boards are used to reduce voltage changes due to varying current demands during the measurement cycle. The capacitor bank includes 330 µF capacitors in parallel (5 on the main and 16 on the auxiliary board) for a total of 7.26 mF.

Several voltages are derived from the supply voltage as shown in Table 1. Three power supply rejection ratio (PSRR) RF linear regulators (AD LT3042) generate three voltages (1.2 V, 3.3 V, and 5 V) with excellent noise immunity. The regulators are always on and have a settable hardware current limit and a programmable power-good output. These three power-good signals are connected to the SF2 for monitoring. The generation of −5 V and 10 V required DC-DC converters. Since the trolley operates in a magnetic field and is making sensitive magnetic field measurements, buck and fly-back converters utilizing inductive components were not considered. Instead, a low noise dual supply with boost-and-inverting charge pumps (AD LTC3265) as well as integrated linear regulators is used to generate the final output voltage. The LTC3265 can be configured to provide different voltages for the boost and inverting charge pumps. It also operates at a single common switching frequency for both outputs and therefore generates only one single source of noise. The LTC3265 converter was set to operate at 500 kHz, which sits far outside the most sensitive frequency range of the NMR mixer (up to 50 kHz). Additionally, the converter includes two low-dropout regulators (LDOs) that were utilized to convert the charge pump outputs of −6 V and 12 V to low noise −5 V and 10 V, respectively. The LTC3265 offers independent controls for its outputs, which are used to turn off the 10 V power outside the NMR measurement sequence.

Two inputs in the 8-channel ADC are used for voltage monitoring. One voltage monitor signal is a divide-by-two copy of the incoming trolley voltage. The second one is proportional to the analog sum of −5 V, 5 V and 10 V, which was implemented through a CMOS op-amp (TI OPA333). Even though the signal is only the sum of three voltages, it is useful for monitoring the behavior of the different power supplies throughout the measurement and whether all supplies are in regulation.

The SmartFusion main board has additional smaller components. One temperature sensor (ADT7420) is integrated with the board and another one is connected to one of the 17 NMR probes. The ADT7420 is a 16-bit digital I^2C temperature sensor and has an accuracy of ±0.25 °C, which is critical to make temperature corrections for a precise NMR measurement. An integrated, low-

voltage barometric pressure sensor (TE Connectivity MS5637) monitors the ~1 bar nitrogen pressure inside the trolley shell. The pressure sensor has an integrated temperature sensor to constantly calibrate the pressure reading. The MS5637's accuracies are ±2 mbar and ±1 °C, respectively.

The SF2 main board also provides several level translators. An 8-bit bi-directional voltage-level translator (TXB0108) is used to convert 1.2 V logic on the SF2 to higher voltages for several purposes. One translator converts to 5 V logic for both the probe selection inside the NMR multiplexer and the switch control of the preamp and mixer power supply. A second translator provides an external diagnostic port with 5 V logic. A third 2-bit level translator (TXB0102D) is used for the control signal for the RF switch, which sends the RF to the RF power amplifier.

2.5.2 Auxiliary board

The auxiliary board provides an interconnect between the main board and the legacy NMR front-end board (A296) through multi-pin connectors on both of its sides. The PCB is shown in Fig. 8. Once assembled, the board houses a bank of sixteen 330 µF capacitors and contains a pair of op-amps that form a single-ended and differential low-pass filter. They were implemented on the auxiliary board to reduce noise pickup from sources like the digital electronics or power supplies.

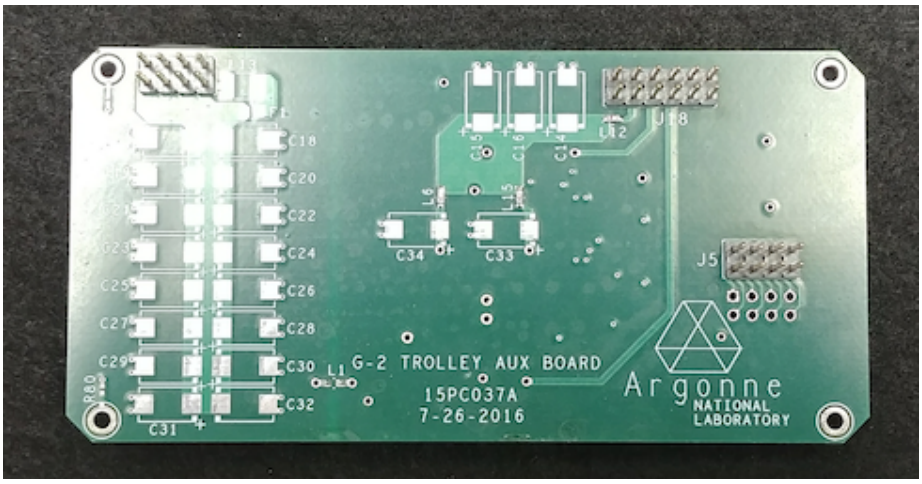

Figure 8: The top of an auxiliary PCB.

The single-ended to differential amplifier uses two fully differential op-amps (THS4521). The first stage converts the single-ended signal into a differential output using a single-pole low-pass filter with unity gain and a 3 dB cut-off frequency of 94 kHz. The second stage is configured as a multiple-feedback, two-pole low-pass filter with unity gain and a 3 dB cut-off frequency of 94 kHz. Its output connects to the NMR ADC input on the main board. The board also includes a 2.048 V voltage reference (REF5020) to add offsets to the differential amplifiers.

2.5.3 Analog board A296

The analog board A296, developed by the University of Heidelberg [9], is shown in its original state from the E821 experiment in Figure 9. The board receives the signal from the NMR preamplifier (see Section 2.5.5) through an SMA connector. This signal is amplified in a first stage on the A296

through an NPN silicon RF transistor (Siemens BFQ69). The amplified FID signal is split and one copy is sent into another BFQ69 configured as a buffer. The signal is then routed into a mixer that is implemented through a dual gate MOSFET (Philips BF981). The second gate of this MOSFET is connected to the 13 dBm, 61.74 MHz precision RF signal received from the main board. The RF signal is also routed into an Adams-Russell gallium arsenide (GaAs) SPDT RF-switch, which is controlled by the SF2. One of the RF switch's outputs is routed to the RF power amplifier (see Section 2.5.4) where it is used to produce the strong $\pi/2$ pulse. The mixed down frequency after the dual gate MOSFET is ≈50 kHz and the signal is amplified with a wide-bandwidth, dual junction gate field-effect transistor (JFET) input op-amp (TI TL082). The amplified output is routed into a 94 kHz filter stage on the auxiliary board.

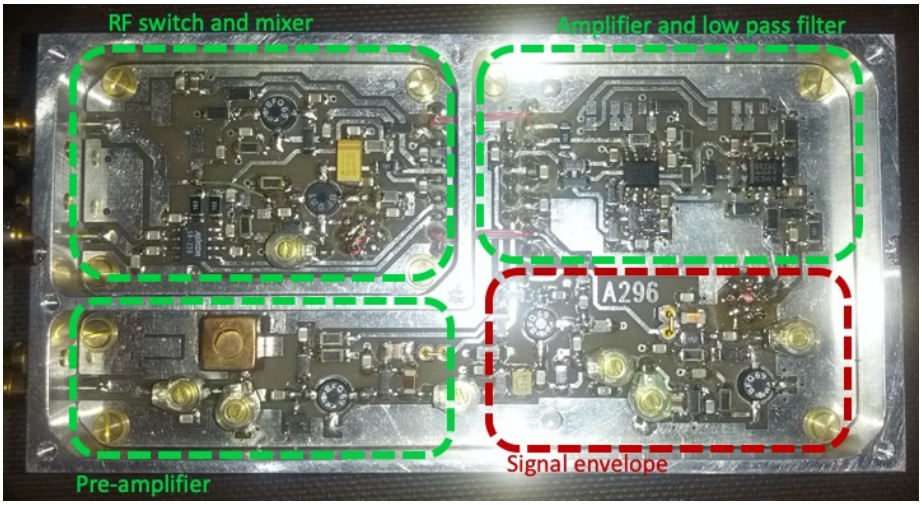

Figure 9: The top of the original A296 before modifications for the E989 experiment were applied. The labeled, dashed boxes indicate the four major board regions and their functions. The green areas are used in E989 whereas the red signal envelope area is obsolete and disabled.

In E821, a second copy of the output from the first amplification stage was routed to a mixer that generated an envelope signal needed for the hardware-implemented zero-crossing counting. In the current E989 system, this signal is obsolete and the stage is disabled on the board.

2.5.4 RF power amplifier

The RF power amplifier inside the trolley is implemented as a Class-C amplifier and is the same as in E821. It is inside its own enclosure on top of the main electronics box and receives a 13 dBm, 61.74 MHz RF signal from the A296 board through a short external cable connection. The amplifier output generates the $\pi/2$ pulse to initiate the NMR measurement sequence (see Section 2.6). The typical pulse length of ~7 μs is programmable and optimized for maximum NMR signal strength.

The amplifier has two stages with a total gain of about 25 dB. The first stage uses a low-power, RF transistor (MRF4427) with a typical gain of 20 dB. Its output connects to a RF power field-effect transistor (FET) (DU2820S) with a typical gain of 11 dB. The two stages are both designed to operate in the Class-C mode for high efficiency (> 70%). Attenuators between the two stages and at the output increase stability, facilitate a broadband output impedance matching to 50 Ω, and

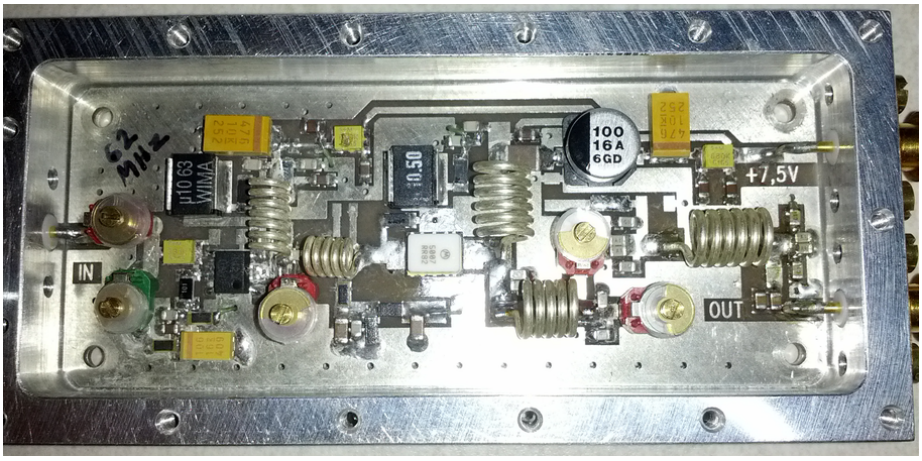

Figure 10: The RF power amplifier.

prevent damage to the transistor in case of a mismatch. The two amplification stages are connected to the 10 V supply voltage through capacitors that stabilize the waveform without decreasing the operating voltage. A low-pass filter at the output was tuned to a cut-off frequency of 96 MHz.

2.5.5 Multiplexer / duplexer and preamplifier

The NMR multiplexer / duplexer unit is separate from the main electronics and RF amplifier enclosures. An NMR preamplifier box is attached to the top plate of the multiplexer / duplexer unit. Both units are shown in Figures 11a and 11b and attached to the probe holder in Figure 12b. The units are used in the E989 experiment without any modifications to their original E821 design. Schematics of the multiplexer / duplexer system were not available so the description here is based on reverse engineering and the assumption that the design followed the similar concept that was used for the fixed probes in the E821 system [11].

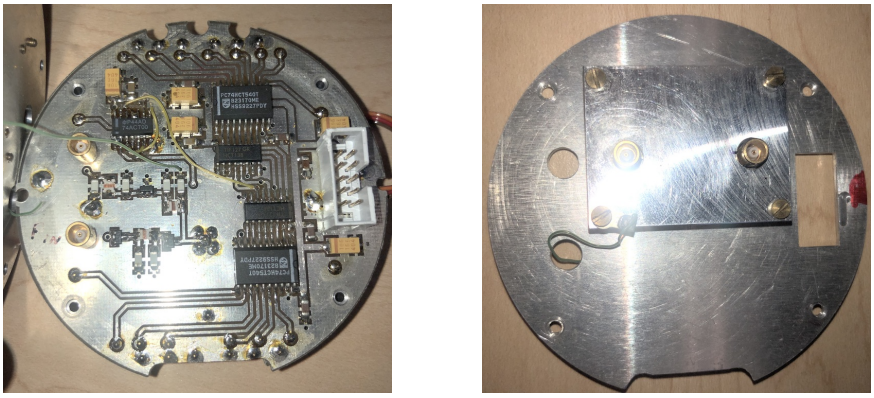

(a) (b)

Figure 11: (a) The multiplexer / duplexer unit with cover plate removed. This is the top board of the unit which mostly comprises the duplexer and parts of the multiplexer. A second board sits underneath. (b) Top plate of the multiplexer / duplexer unit with the preamplifier box attached to it.

The ~5 W, $\pi/2$ pulse from the RF power amplifier is received via a short coaxial cable and fed into the duplexer. A pair of crossed diodes turn into a short circuit for the strong RF pulse while they are high impedance to the subsequent weak NMR pulse. The RF pulse hence passes through to the multiplexer where it connects to all input ports of all 17 probe channels. However, only one of these is active through a current signal sent to this channel (similar to the principle described in [11]). The selection of the channel is achieved via five address bits sent as TTL control signals from the SF2 on the main board to the multiplexer. These five address bits are connected to pins on two 3-line to 8-line decoders (74HCT138) and one quad 2-input NAND gate (74ACT00) that generate the signal to select a specific probe.

While the strong $\pi/2$ pulse is routed to each selected probe, the returning weak NMR signal can similarly pass through the selected channel of the multiplexer. It is blocked by the pair of diodes and does not go to the RF amplifier output. Instead, a second route in the duplexer (similar to the design in [11]) is available and comprises two $\lambda/4$ sections that combine to a $\lambda/2$ line for the NMR signal. This allows the routing of the weak NMR signal to the preamplifier. A second pair of crossed diodes turns this into an effective $\lambda/4$ element for the strong RF pulse. The high impedance of this leg reduces the voltage at the preamplifier during the $\pi/2$ pulse and with it its dead time.

The NMR preamplifier [9] is unchanged from E821. It has an input and output impedance of 50 Ω and a total gain of 20 dB. A first 30 dB gain stage is implemented with an NPN silicon RF transistor (BFQ69). A second filter stage with an attenuation of −10 dB forms a band-pass with a frequency range of 55-70 MHz. The preamplifier output is routed via a short cable to the A296 board for further amplification and signal processing.

2.5.6 Probes and holder

For the E989 experiment, a new probe holder was designed (see Figure 12a) with new features that are beneficial for the trolley field measurement. The multiplexer unit rigidly attaches with screws to the new holder to keep its distance to the probes fixed. The new design has recessed holes in the endplate instead of through holes. The probes therefore mechanically stop in the same azimuthal position when inserted into their slots. Set screws hold each probe fixed in their positions.

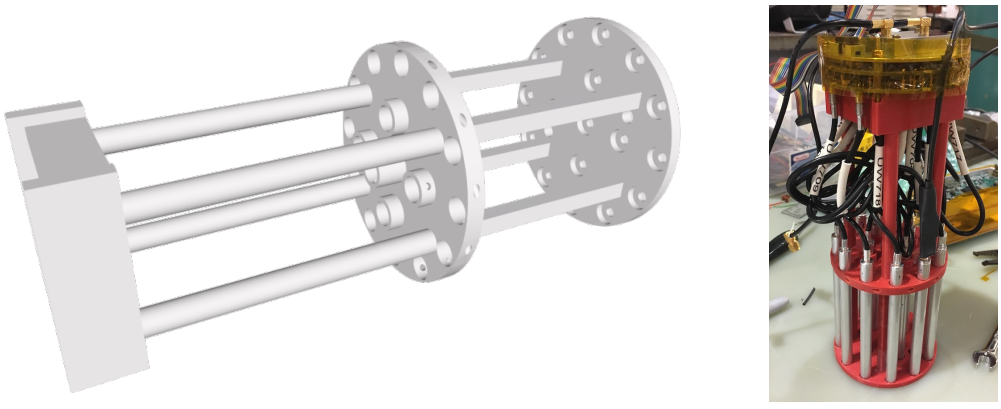

(a) (b)

Figure 12: (a) The design drawing of the new 3D-printed probe holder. (b) The new 3D-printed probe holder with the 17 NMR probes and the multiplexer mounted.

Figure 12b shows the new, 3D printed probe holder with the multiplexer unit attached and the 17 new NMR probes mounted in their slots. These probes were developed by the University of Washington and are similar to the fixed probes mounted on the outside of the storage ring vacuum chambers. The probes' active volumes are filled with petroleum jelly. An external temperature sensor (ADT7420) is attached to the crimp connection of the cable at the end of probe #12.

The curvature of the trolley shell has been incorporated into the probe holder so that it can be easily slid inside the trolley. The rotation around the long axis is hence limited. A marker on the front plate indicates the relative orientation around this axis.

2.5.7 Barcode reader

The new barcode board (Figure 13) is attached at the bottom of the trolley shell and resides in vacuum. It is mounted on standoffs to adjust the distance of the photo diode and sensor elements to the barcode marks. A 10-pin vacuum-feedthrough in the trolley shell connects the 10 signal lines between the main board and the barcode reader. Three lines are for −5 V, 5 V, and ground. One channel provides an LED voltage (LED_CTL), which is set by the SF2 through the DAC of the 8-channel ADC on the main board (see Section 2.5.1). The remaining six channels are the readout signals from the reader elements that go to the 8-channel ADC.

Figure 13: The barcode reader board top and bottom view.

The barcode board is a new design for the E989 experiment and includes two different groups of barcode readers which are separated by about 12.5 cm. This maintains continuity of a position readout over discontinuities in the barcode marks between structures of the $g-2$ vacuum ring. Each group has three separate reader elements: clock (CLK), direction (DIR), and position (POS) as shown schematically in Figure 14. The CLK and DIR reader elements record the regular pattern of dark and bright stripes, which have an average width of about 2.08 mm. Since the elements are offset, they act like a quadrature incremental encoder and give both a position and direction of the trolley movement. The POS reader is monitoring the radially offset absolute patterns. These marks have an azimuthal spacing of ∼12.5 cm and contain 12 marks each. The first and last one are always dark stripes that indicate the start and stop bits. The ten spaced stripes between them form bit patterns that reflect unique numbers around the entire storage ring. These absolute marks allow the determination of an absolute location of the trolley around the ring.

A single reader element comprises a high-speed, infrared-emitting (940 nm) LED (Vishay VSMB2000X01) and two red-enhanced photodiodes (Advanced Photonix PDB-C154SM) as the

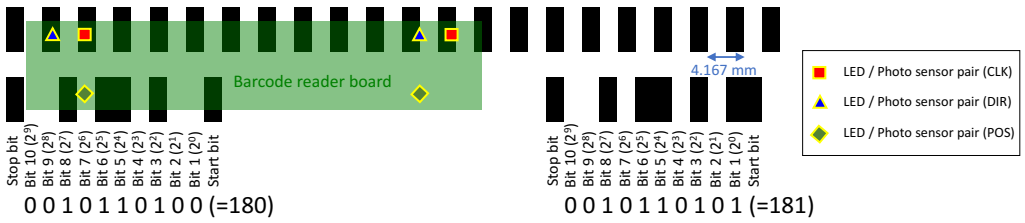

Figure 14: Schematics of the barcode principle with the two reader groups consisting of three readout elements (CLK, DIR, POS). The CLK and DIR elements are measuring the regular barcode marks and the POS registers the absolute marks spaced every ∼12.5 cm. These marks form unique bit patterns. The curvature of the marks following the storage ring was omitted here.

light sensor. The infrared wavelength optimizes the reflection from the aluminum cage and the barcode marks. The output of a rail-to-rail, high output drive op-amp (TI TLV4111CDGN) drives the three LEDs from one group in series with a 1 kΩ resistor. The op-amp's positive input terminal is set by the LED_CTL voltage control signal. The negative input is connected to the 1 kΩ resistor. Therefore, the LED voltage really sets the current through the resistor and the current through the three LEDs. The typical current is 1 mA since the voltage across the resistor is limited to the difference between the 5 V supply and the sum of the three LED forward voltages of ∼4 V.

The photodiode pairs are reverse biased with the cathode at virtual ground and anode at −5 V through a 10 kΩ current limiting resistor. The current from each photodiode pair is read out with an amplifier (TI OPA381) that operates off a single 5 V rail to reduce power. The amplifier's input, with a single positive rail, functions all the way to ground. For improved linearity at ground, a 10 kΩ resistor was added from the output to the −5 V rail.

2.6 Control firmware and software

The control firmware and software handle the run state, data digitization and transmission, monitoring of the system power, and the control of the TDM in the SCC. On the interface side, a Xilinx Zinq-7000 SoC is used, whereas a low-power SF2 is used in the trolley. In nominal run conditions, each NMR probe in the trolley is read out twice per second, which requires switching the SCC with 34 Hz between communication and RF transmission. The monitoring of the power in the interface and the trolley, the barcode trace digitization, and timestamp generation operate continuously as they are independent of the NMR measurement and data communication cycles. This continuous activity is outlined in Section 2.6.1. All electronics associated with communication and NMR measurements operate in the corresponding 29.4 ms long sequences as described in Section 2.6.2.

2.6.1 Continuous activity

Only three processes run continuously on the trolley: the operation of the trolley's local timestamp counter, monitoring of the power-good status and operation of the 8-channel ADC which reads the barcode and monitors the voltages. After each communication cycle or when not otherwise directed by the interface, the trolley will continuously listen for the next command frame.

The readout of the ADC still depends on the communication cycles. The digitized data from the 8-channel ADC, with its maximum sampling rate of 1 MSPS, is stored cycle-wise in a buffer

and processed at the cycle end for packaging. The sampling period is pre-scaled on the trolley side to reduce the raw data volume. A sampling rate of 10 kSPS is typical. As mentioned before, the eight channels of the ADC store the values of all three photo sensors for each of the two barcode groups and two on-board voltage signals as described in Section 2.5.1.

Timestamps Independent of the NMR sequences, a local 64-bit timestamp running at 20 MHz is available in the trolley as well as in the interface. These timestamps are used to tag the time of the various on-board measurements. In addition, a GPS synchronized timestamp is available on the interface. The 100-bit long IRIG-B data frame provides an absolute date. Xilinx digital signal processor (DSP) cores are used to convert this date into a 64-bit Unix universal time coordinated (UTC) timestamp in nanoseconds synchronized to the 10 MHz reference clock from the SRS. The timestamp increments on both edges to provide 50 ns timing resolution. If the external IRIG-B signal is not available, an internal clock is used instead. A 40 MHz GPS-synchronized timestamp is recorded by the trolley interface at the start of each communication cycle.

Protection On the interface side, the digitized voltages and current of the trolley power supply are constantly monitored at 125 kSPS. To protect the trolley electronics, the power and RF are switched off if the measured values exceed predefined limits. Furthermore, the power output is disabled if a large voltage but negligible current are measured, which indicates a disconnect of the SCC cable.

2.6.2 Trolley NMR sequence

The sequencing of different subsystems is handled by finite state machines running at 1 MHz. A cycle in which the NMR system is operated consists of the following tasks: i) sending commands through the SCC (see Section 2.6.2), ii) switching the cable's connection between the coax driver and the RF system through the RF switches in the SCC, iii) toggling the RF switch on the A296 board to create a proper $\pi/2$ pulse for the NMR systems, iv) multiplexing to the desired NMR probe, packaging the data of the digitized FID and auxiliary sensors, and v) transmitting data frames. On the interface side, additional trolley power supply and RF monitoring information in combination with a UTC timestamp from the cycle start are merged into the outgoing data stream. Figure 15 gives an overview of the timing of the different systems for one such measurement cycle.

Interface - trolley communication Data and command frames are received and transmitted through the SCC, and the phase is detected using a six-fold oversampling of the 40 Mbit/s bitstream. A 16-bit payload word is encoded into a 20-bit, providing data frame alignment and error detection.

An interface command frame consists of 32 16-bit words of settings and potentially additional data that can write setting and data information to the trolley on-board flash memory. Every data frame is trailed by a cyclic redundancy check (CRC) check sum.

NMR sequence control In each cycle mentioned above, one NMR probe is pulsed and read if enabled. The probe selection in each cycle is determined by the received command and is managed through common registers. An NMR sequence consists of multiplexing to the desired NMR probe, emitting the RF $\pi/2$ pulse, enabling the preamplifier for the FID signal, and enabling the on-board ADC to digitize the corresponding signal. The timing of this sequence is managed through common

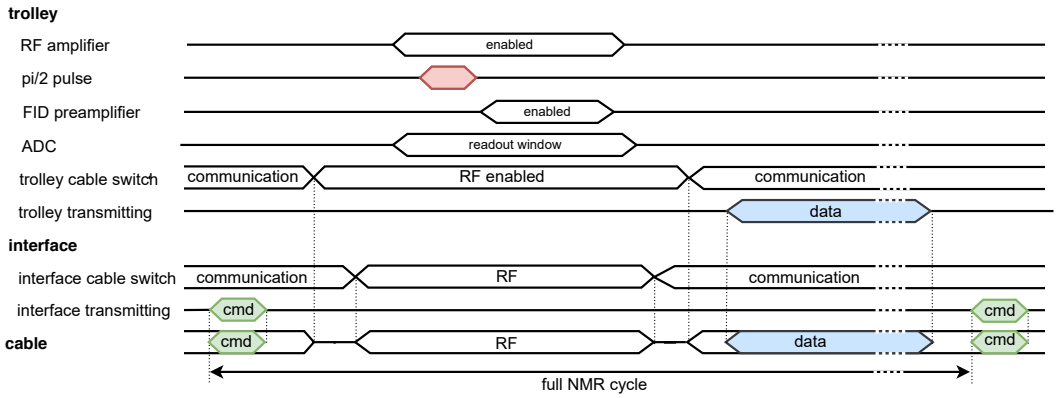

Figure 15: The scheme of the trolley and interface communication and control sequences. The dashed horizontal lines indicate an abbreviated representation. The cable's mode can be understood as an "xor" of the cable switches of the trolley and the interface as indicated by the vertical dotted lines. Commands (cmd) and data can only be exchanged when both switches are in *communication*-mode. The RF is only transmitted successfully to the trolley if both switches are in *RF*-mode.

registers modified by the received commands and controlled by a state machine. A nominal prescale of 62 leads to a ~1 µs timebase. A typical sequence is as follows, the ADC is enabled 300 µs before the RF pulse ($\pi/2$ pulse) that has a length of 7.25 µs. The FID preamplifier turns on 6 µs after the end of the RF pulse for a duration of 14 ms; After which the ADC stays active for an additional ~1 ms to obtain a second baseline measurement. Since the ADC runs in the RF clock domain with a sampling speed of 996 kSPS (see Section 2.5), a clock domain transition is required. An on-board 50 ns-timestamp is assigned to the time of the first sample of the FID digitization.

Auxiliary sensors and measurements The RF power in the trolley and the interface are monitored by two comparators at a 50% and 66% with respect to 13 dBm (see 2.5.1). The duty cycle of both comparators, sampled at 40 MHz, during the time in which the RF is enabled is calculated for each cycle. The comparison of the two duty cycles yields a proxy for the RF power. The auxiliary temperature and pressure sensors are read out once a cycle on request through I^2C.

Data packaging and transmission At the end of the cycle, all the available data is collected and transmitted through the SCC to the interface. This data frame consists of:

- a preamble for initial synchronization of the trolley interface to the bit stream,
- status flags and the NMR probe number of the cycle,
- temperature, pressure, voltage, and RF power readings from monitors,
- on-board timestamps of the cycle start or "measurement" cycle, the timestamp corresponding to the first NMR waveform sample, and the timestamp corresponding to the first barcode ADC sample,
- barcode configuration readbacks,

- a copy of the commands sent from the interface to the trolley,
- the NMR FID samples including checksum,
- all barcode ADC samples acquired during this cycle,
- the readback from the flash memory (optional), and
- a 32-bit frame checksum.

The number of transmitted samples from the digitized FID and the barcode ADC can vary slightly because they run in independent clock domains. For a typical setting of 16,000 FID samples and 2,000 barcode ADC samples, data frames of 64,194 bytes are transmitted. While the number of barcode samples may vary, the trolley will always report the timestamp corresponding to the first sample such that the date can be reassembled and correlated with other measurements.

Data interface In addition to the above-discussed data frames, the data stream from the interface contains dedicated interface frames. They contain status bits, a GPS timestamp for the cycle start, a local timestamp, the minimum and maximum of the digitized voltages, currents, and the RF power, and the voltage and current traces.

2.6.3 Software control

In the Muon $g-2$ experiment, the data acquisition, run control, and hardware control is based on the Maximum Integrated Data Acquisition System (MIDAS)[8]. Basic functions, such as data logging and run transitions, are handled by MIDAS while users need to develop their specific front-end functions that actually communicate with the hardware. For the trolley system, such a front-end program was developed that interacts with the trolley interface. The front-end acquires data frames from the interface and writes control commands to the interface at the beginning of a run or upon a user request. A user-friendly, web-based control page was developed for adjusting control parameters. The page also displays real-time readbacks of status parameters.

At the start of each run, a predefined number of NMR cycles (usually five) are performed without the RF pulse to monitor and record the baseline for systematic studies. Typically, a new run is started whenever the trolley starts a new motion. A nominal, complete field scan of the storage ring results in a single run that takes roughly 1 hour. An online analysis program has been developed using the Art event processing framework[9]. This program fetches the most recent data from the MIDAS system, unpacks the data, performs analysis, and displays the result on web pages. The values rendered on these pages include NMR signals from each probe, the signal from each barcode reader, trend plots of the NMR probe frequency extraction, and status monitoring parameters.

3 Trolley mechanical and motion control system

3.1 Overview of the mechanical and motion control system

The design of the trolley motion system is guided by four primary requirements: i) preserving the vacuum environment of $<1 \times 10^{-6}$ Torr, ii) minimizing magnetic perturbations in the muon storage

[8] https://midas.triumf.ca/MidasWiki/index.php/Main_Page
[9] https://art.fnal.gov/

region, iii) minimizing disturbance to the behavior of stored muons and their decay positrons, and iv) reliably deploying the trolley to fully map the magnetic field around the ~14 m diameter storage ring in a maximally automated way. Critical to meeting the requirement of the reliable operations is the design of the mechanical systems with sufficient clearance to avoid interference with the nearby subsystems including electrostatic quadrupoles, magnetic kicker plates, and beam collimators.

To meet the environmental requirements of low vacuum load and minimal magnetic influence, the dominant construction materials of the trolley mechanical systems are aluminum and copper. This follows the general approach of the experiment so that the vacuum load and magnetic field gradients near the trolley motion systems are not significantly distinct from other areas of the ring.

The important elements of the trolley motion system are the drive station and the garage system. The drive station controls and monitors the azimuthal motion of the trolley, while the garage moves the trolley from the muon storage volume into its parking position located outside the beam and decay paths. Figure 16 shows an overview of the muon storage ring with the locations of the drive and garage systems along with an indication of the trolley motion path during its measurement. The trolley is inserted into the storage region by the garage mechanism. The trolley drive mechanism pulls the trolley clockwise from the garage (ϕ = 175°) towards the drive (ϕ = 262°) followed by a full scan counterclockwise from one side of the drive to the other. The trolley measurement is completed by the return path from the drive to the garage in the clockwise direction. Finally, the garage system moves the trolley to the parking position.

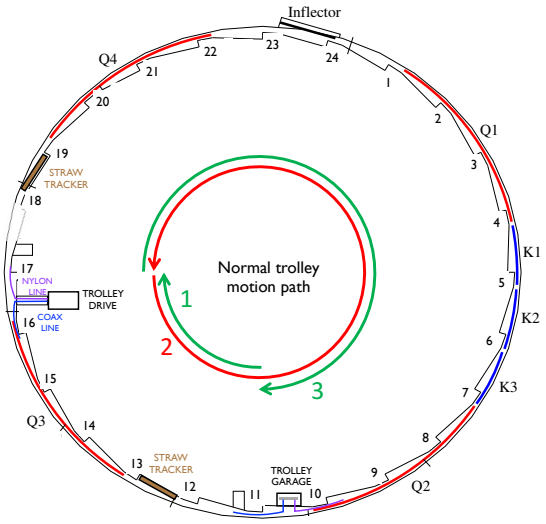

Figure 16: Overview of the Muon $g-2$ storage ring with the trolley drive and garage systems and other critical systems. The labels Q, K, and 1-24 refer to the electrostatic quadrupoles, magnetic kicker, and calorimeter stations, respectively. The trolley motion path during its normal measurement cycle is indicated by the green and red arrows in the center of the schematic.

The trolley motion system was developed by the University of Heidelberg for E821. For cost efficiency, only the electronics systems were fully replaced by Argonne National Laboratory, while the mechanical system was refurbished with minimal changes. A schematic view of the new motion control system and the mechanical systems are shown in Fig. 17. The mechanical systems of the

trolley drive and garage are detailed in Sections 3.2.1 and 3.2.2 and the motion control system in Section 3.3. The motion control system also operates the in-vacuum, calibration NMR probe [12].

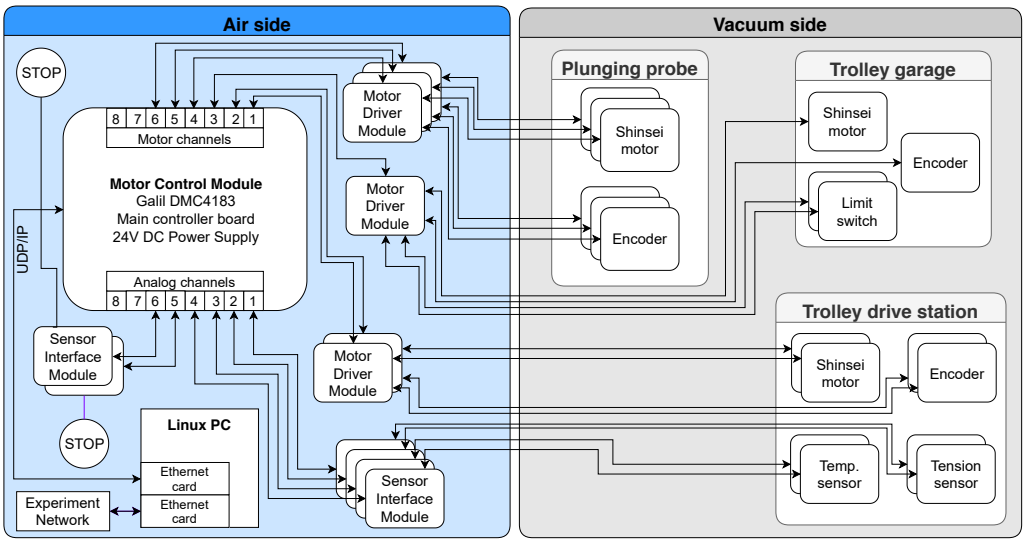

Figure 17: Schematics of the trolley mechanical and motion control systems.

3.2 Mechanical systems

3.2.1 Drive station

The motion of the trolley is controlled by two cables pulling the trolley azimuthally from opposite sides. One cable is the coaxial signal cable (see Section 2.4.1), and the other cable is a heavy-duty nylon line. The drive station is a vacuum chamber that contains the cable driving system shown in Figure 18a. It is located ~2 m from the storage-ring vacuum chamber to minimize its field perturbation at the muon storage region.

The cables are wound inside the drive onto two 50 cm-diameter drums. The drums are 25 cm wide and have spiral grooves that guide the cables during the (un)winding. As the drums rotate, a cable guide consisting of two oppositely moving pulleys ensures that the cables are guided onto the grooves smoothly. A top view of the drums together with the cable guide mechanism is shown in Figure 19. At the end of the spiral groove, a hole routes the cable to the drum's interior. A knot on the nylon cable inside the drum prevents it from slipping back through the hole. For the signal cable, a metal clamp holds it in place. The coaxial cable is then connected via an SMA connector to a thinner coaxial RF cable, which has a smaller minimal bending radius. This thin cable is routed out of the drum through a hole at the center of the drum, it is then connected to the signal cable outside the cable drive chamber through an isolated SMA feedthrough. As the drum rotates, the thin cable is wound onto the drum axle. To prevent knots in the thin cable, five pairs of spring loaded pulleys guide the cable winding as shown in Figure 18b.

The cable drive connects to the storage ring vacuum chamber through two 3 mm-diameter tubes. These tubes allow the cables to pass through while limiting the conductance between the storage ring vacuum and the cable drive vacuum. Before the cables enter the connecting tubes, each cable is wound across three pulleys to form the tension sensing mechanism as shown in Fig. 19.

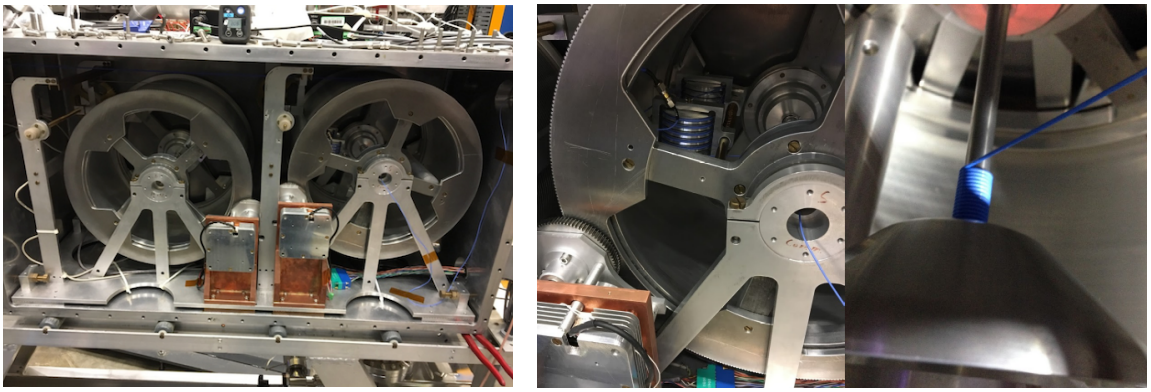

(a) (b)

Figure 18: (a) The cable drive chamber without cover showing the two cable drums, two motor holder stands with motor enclosures and copper heat sinks, and the new gear boxes connecting the motors to the drum gears. (b) Close-ups of the cable winding system for the signal cable. The coaxial signal cable is guided out of the cable drum through a hole where it connects to a thinner blue coaxial cable. The spring loaded pulleys visible in the left close-up keep this thin signal cable tight and guide its (un)winding around the drum axle as shown in the right part of the picture.

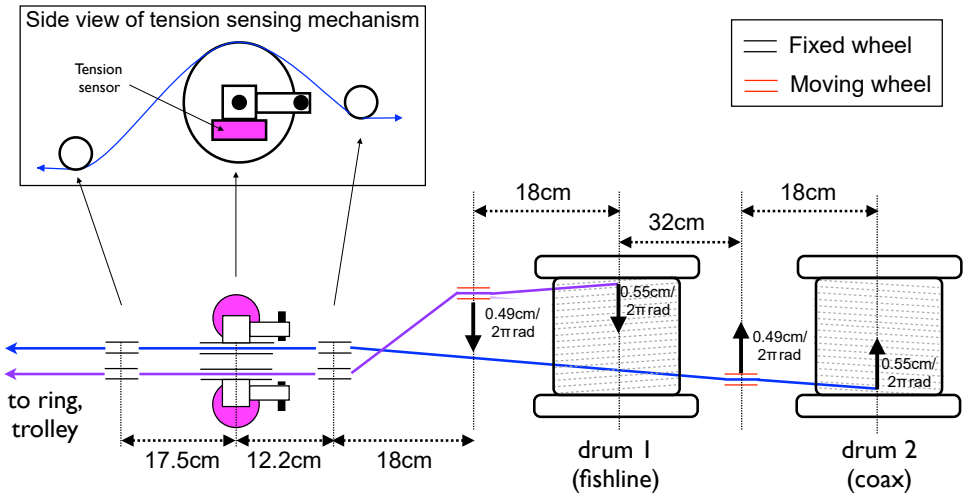

Figure 19: Top-view illustration of the trolley drive pulley system with an inlet side view of the tension sensing pulley. Main dimensions are indicated as the schematic is not to scale.

The middle axle attaches to a rotating arm so that the wheel can both rotate and move up and down freely. A block mounted to the wheels axle rests on a tension sensor (Burster 8523-200N). The two tension sensors' values are converted in a Sensor Interface Module (SIM) (see Section 3.3.5) to be used by the Galil controller (see Section 3.3) for motion regulation. The coax cable was tested by the manufacturer to withhold up to 89 N of tensile force. The tension values are also used to implement software and hardware limits far below this threshold to prevent damage during operation.

Gear teeth on the edges of each cable drum engage with a non-magnetic, Shinsei piezo-electric

motor (USR60-S3N). The two drive motors are connected to a Shinsei motor driver (D6060). The USR60-S3N motors have a maximum torque of 1 N m and an optimal speed range from 60 rotations per minute (RPM) to 120 RPM. To achieve the normal trolley speed of ~1 cm/s and be in the recommended RPM range, a gear box was added between the motor and the drum gears.

Since the new USR60-S3N motors have the same form-factor as the E821 motors, they fit into the existing holding structure without major modifications. The motors are held by a copper heat sink and aluminum housing. Thermal paste is applied at the interfaces to the enclosure and heat sink to improve heat conductance inside the vacuum chamber so that the motors remain below the recommended maximum operation temperature of 55 °C. Temperature sensors with direct contact to the motor shells were added in the E989 experiment. During the typical 3-hour trolley operation, the motors' temperatures do not exceed 39 °C. The cable drums are also engaged with incremental rotary encoders from Allied Motion (CP-850-1000-3/8-F-A). This provides a recording of the drums rotational position, which produces a measure of the trolley's azimuthal position.

The cables for the motors, encoders, and tension and temperature sensors are connected to a 41-pin vacuum feedthrough on the wall of the drive chamber from where they are routed to their respective electronics (see Sections 3.3.4 and 3.3.5).

3.2.2 Garage

During periods of muon injection, the trolley is ~30 cm away from the path of the muons and decay positrons. After completing each field map, the trolley is retracted in the radial direction by a system of mobile support rails into the so-called trolley garage, shown schematically in Fig. 20. The garage motion is driven by a Shinsei piezo-electric motor (USR60-E3NT), which comes with its own incremental encoder. The motor is connected to a Shinsei motor driver (D6060E). Since the motion control system reacts based on the encoder readbacks, the Shinsei driver's internal speed control was disabled with a jumper.

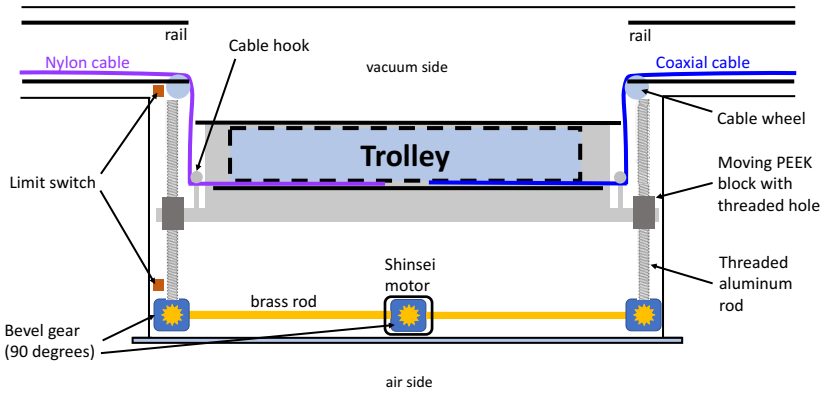

Figure 20: Schematic top view of the trolley garage system.

Using the motor, a gear box, and threaded rods, the garage apparatus radially moves a segment of the trolley rails. When the trolley is parked on this section, it can be radially moved as well. Cables from the motor, encoder, and limit switches connect through vacuum feedthroughs on the garage flange to air-side electronics (see Section 3.3).

Because the trolley is connected to the nylon and signal cables, the motion of the garage has to be synchronized with motion of the drive drums. The drums have to release the cables when the trolley is being pulled into the parking position. During the trolley insertion into the muon storage region, the drums retract the cables. The cable drum motion maintains and regulates the tensions in the cables. There are two cable hooks on each side of the mobile rail section that keep the trolley driving cables parallel to the trolley body during the garage motion. Two cable wheels at each end of the fixed rails provide a smooth curvature for the second 90° bend of each cable. It is also important to ensure that the mobile rail section is aligned with the rest of the trolley rails at the end of the insertion process so that the trolley can smoothly drive over the rail gaps. An optical limit switch was mounted close to the storage region to indicate when the mobile and fixed rails are aligned. A second limit switch defines the parking position of the trolley. The garage flange has two optical windows. On the atmospheric side of the windows, two 3D-printed, light-tight boxes each house an LED and camera to visually monitor the trolley and garage rail operation remotely.

3.3 Motion control system

3.3.1 System overview

The key element of the motion control system is the custom-built Motor Control Module (MCM) shown in Fig. 21, which is centered around a commercial, 8-axis motion controller (Galil DMC-4183) as shown in Figure 22. The Galil module executes the motion command scripts and controls the motors based on their encoder and tension readbacks. The MCM also contains a custom-built main controller board for supplying voltages to the motors and transmitting control and receiving readback signals. Because the motor control voltages of the Galil and the Shinsei motor drivers are incompatible, custom built Motor Driver Modules (MDMs) facilitate the translation of signals. The MDM integrates the Shinsei motor drivers and a custom board for signal conversion. The MDM interfaces with the Shinsei motors, encoders, and limit switches, and communicates with the Galil system through the main controller board. The system built for the E989 experiment uses a total of six motor channels; three for the 3D movement of an NMR calibration probe, two channels for the trolley drive, and one for the garage mechanism. This leaves two channels as hot spares.

The MCM was built with eight analog input channels that connect to the Galil's eight ADC channels. A custom-built SIM provides the interface between the MCM and the individual sensor. Four of these analog channels are used for reading out two tension sensors and two temperature sensors that are installed in the trolley drive. Two channels are connected through two SIMs to emergency stop buttons. The main components of the MCM will be described in Sections 3.3.2 (Galil) and 3.3.3 (main controller board). Sections 3.3.4 and 3.3.5 explain the design and functionality of the MDM and SIM, respectively. Section 3.3.6 details the control software and motion scripts that are used to perform the motion of the trolley and the calibration probe.

3.3.2 Galil motion controller

The motions of cable drums and the garage are controlled by an 8-axis Galil DMC-4183 motion controller, which is integrated into the MCM as shown in Fig. 22. Its main functionality is to read the positions of the various motors through their rotary encoders, monitor the tensions of the cables, and send control voltages to the motor drivers for the requested movement. It precisely controls

(a) (b)

Figure 21: (a) Front and back view of the MCM. (b) Top view of the MCM without cover showing the main components of the Galil controller and the custom-built main controller board.

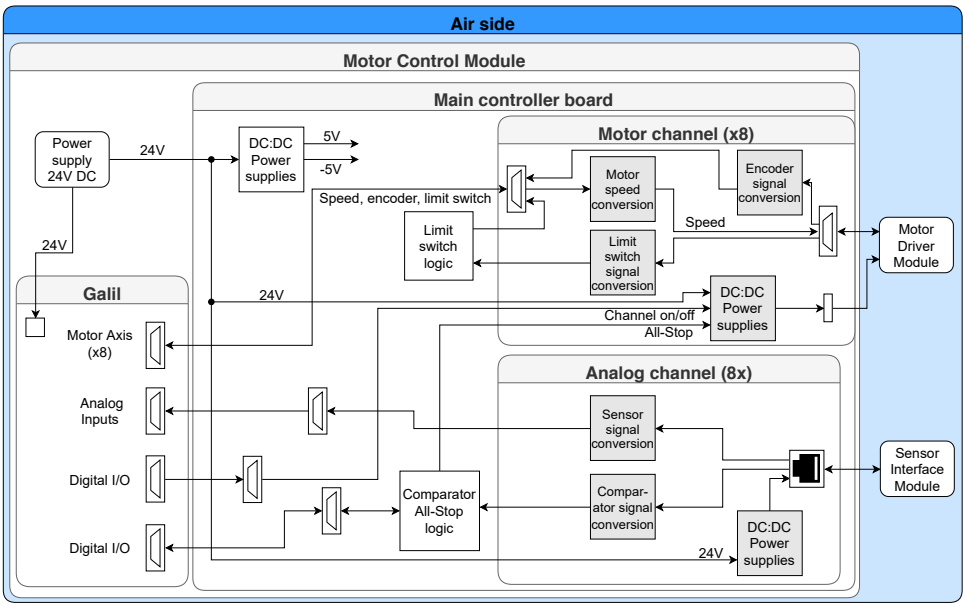

Figure 22: Schematics of the motor control module. Grey shaded boxes in the motor and analog channels indicate elements with galvanic isolation of grounds.

the motor to move to a specified encoder reading, maintains a constant motor rotation speed, or realizes more complicated motion schemes involving other motors through user-defined scripts.

The Galil system communicates with the frontend computer through Gigabit Ethernet via UDP/IP. Interface functions are provided by Galil as a C++ library. To perform its functions properly, the Galil is connected to the main controller board described in the Section 3.3.3. Each axis connects to this board via 26-channel cables with high density HD-DB26 connectors. These cables route the signals for the motor voltage, enable controls, the encoders, and limit switches. A HD-DB15 cable connects the analog channels of the main board to the eight analog inputs on the Galil. Two HD-DB44 cables route digital I/O signals for the axes 1–4 and 5–8 between the Galil and main board. On the Galil side, these connectors also provide access for additional limit switches. The Galil is powered from a 24 V power supply (PMC-24V600W1BA) that is part of the MCM.

3.3.3 Main controller board

The Galil's interaction with the Shinsei motors, their drivers, and other sensors required a custom-built main controller board to provide signal conversion, experiment-specific logic, and galvanic isolation of the Earth and system grounds. The main elements of this controller board are shown in Fig. 22 and comprise the eight motor channels, eight analog channels, and comparator and limit switch logic. Potential ground currents during the field scan may perturb the field and introduce systematic uncertainties. Because the motors inside the trolley drive and garage are in contact with the grounded chambers, a galvanic isolation of all system grounds for motors and analog sensors inside the MCM was introduced. All isolated elements are shaded gray in Fig. 22 and will be mentioned again in the details below. The two ground domains are connected via a 1 MΩ resistor.

The Galil's ±10 V motor speed control signal is routed to a motor channel and attenuated to ±2.5 V. It is then isolated with a unity-gain precision isolation amplifier (ISO122U). The attenuated input signal matches the full output range of the ISO122U with the available ±5 V power supply rails. The single-ended output of the ISO122U is driven out by a differential amplifier (AD8132) with a fully differential output of ±1.6 V in preparation for the required signal for the Shinsei driver in the MDM described in Section 3.3.4. The motor speed output signal is routed via a 16-channel cable to the MDM together with ground, encoder, and limit switch signals.

The LVDS encoder and limit switch input from the MDM are received on the galvanically isolated side and translated into TTL signals (TI DS90C402). The TTL outputs are routed to digital isolators (TI ISO7820F). The encoder signals are connected directly to the Galil through the DB26 cable. The limit switch signals, normally high, are used as inputs to open collector outputs that are routed to a limit switch logic block. The eight forward and reverse limit switch signals of all motor axes are input to a logic bus where they can form a logic OR for each channel individually. Any motor can be set to react to any combination of limit switches through two blocks with eight jumpers for each motor. The outputs of the ORs are routed to the Galil over the DB26 cable where they can be used in the control scripts.

The Shinsei motor driver requires 24 V for the operation and ±5 V are needed in the MDM for logic switches and the analog speed control. These voltages are all generated from the primary 24 V. The 24 V isolation for the MDM is facilitated by an isolated DC-DC converter (Murata Power Solutions UWE-24/3-Q12PB-C). This converter can be controlled via an enable signal from the Galil or the All-Stop signal generated in the comparator logic of the analog channels described below. The ±5 V on the isolated side are generated via isolated DC-DC converters (GE

SHHD003A0A41Z). Each of these two converters receives a control signal (Channel on/off) from the Galil to turn the ±5 V on/off for each channel.

The main controller board also incorporates eight analog channels which provide isolation between the connected SIM from the primary side. The interface connector of the analog channel is a RJ-45 CAT 5E used to provide both ±5 V to the SIM and to receive the differential analog and comparator outputs from the SIM (see Section 3.3.5). The differential analog signal from a SIM is terminated into 100 Ω and received by a differential to single-ended amplifier (AD8130) set to unity-gain. The single-ended output is then connected to the primary side via a precision isolation amplifier (ISO122U) with a full range of ±2.5 V. The output signal is routed via the DB15 cable to one of the eight ADC channels on the Galil.

Each SIM sends an LVDS comparator signal indicating an out-of-range hardware state. This signal is converted in the analog channel to TTL with an LVDS receiver (TI DS90C402). The output of the receiver is connected to the primary side with a single-channel digital isolator (ISO7810F). This output connects to the comparator All-Stop logic block on the main controller board. Each of these comparator signals represents an out-of-range signal for the specific analog channel. The comparator logic block has eight flip-flops (TI SN74LVC1G74) to latch the incoming comparator signals. The latched outputs from these flip-flops are used as inputs for a programmable TTL logic chip (TI CD4048BM), which is configured as an eight-input logic AND. Its output drives the All-Stop control signal sent to the 24 V power supplies. A copy of each comparator channel and the All-Stop signal are connected to the Galil via one of the DB44 I/O cables. The All-Stop output signals are normally high and are buffered by bipolar junction transistors (BJTs) (MMBT2222AL). Each of the latched outputs can be excluded from the AND by adding a jumper to a jumper block integrated to the comparator All-Stop logic. The Galil can reset and override the latches.

Like the motor channels, each analog channel also has local, isolated generation of ±5 V via DC-DC converters (GE SHHD003A0A41Z). The same type of DC-DC converters are used to generate ±5 V on the primary side of the main controller board.

3.3.4 Motor driver module

The Shinsei motors are directly powered and controlled by a driver module from Shinsei. The Motor Driver Module shown in Fig. 23a is a custom-built module that contains this motor driver and a custom board, which was mainly designed to translate the bipolar ±10 V Galil motor speed signal into a unipolar 0 to 3.2 V signal with clockwise and counterclockwise direction controls. The MDM has two input connectors that are connected to the MCM; one cable provides the supply voltages, and the other addresses the motor speed control as well as five LVDS outputs for the encoder and limit switches. Four connectors for the motor, encoder, and forward and reverse limit switches are located on the back of the MDM.

A differential amplifier (AD8130ARM) converts the incoming ±1.6 V signal into a single-ended ±3.2 V signal. The single-ended output of the amplifier then takes several paths. One copy of the output signal couples directly into an analog 2-to-1 multiplexer (AD8180). A second copy is inverted using an amplification stage (TI OPA209) and connects to the second input of the multiplexer. The output of the analog switch is inverted and buffered by an OPA209, which is the translated motor command signal connected to the Shinsei motor driver.

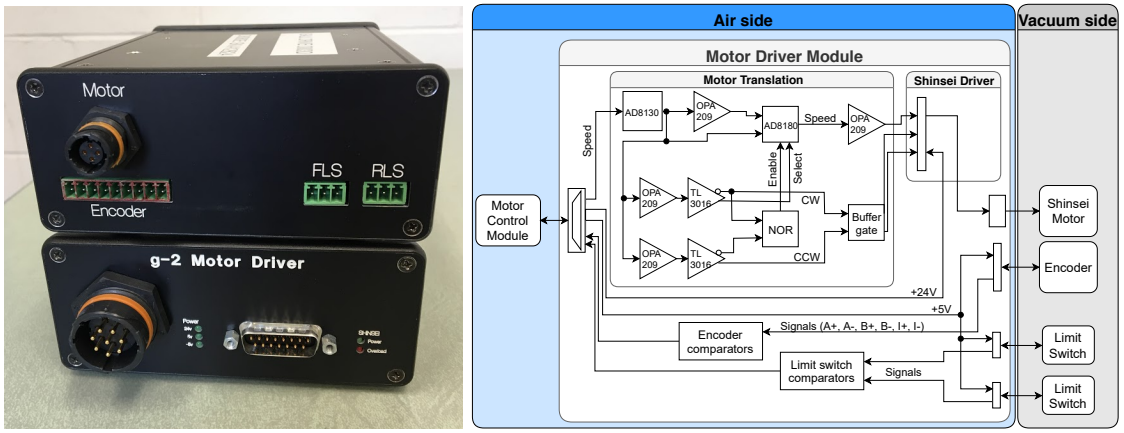

(a) (b)

Figure 23: (a) Front and back panels of the MDM enclosure and (b) its simplified schematics.

The choice of the two analog signals is determined by a set of comparators. A copy of the output of the AD8130ARM amplifier is buffered by a pair of amplifiers (OPA209) and fed into a pair of comparators (TI TL3016) that have thresholds of about 200 mV and −100 mV, respectively. The non-inverted output of the −100 mV-threshold comparator is fed into the channel select of the multiplexer to always provide a positive motor speed signal to the Shinsei driver. The inverted output of the same comparator provides the clockwise (CW) signal for the Shinsei driver, while the normal output of the other comparator generates the counterclockwise (CCW) signal. The CW and CCW signals are buffered through a dual buffer gate (TI SN74LVC2G34) and then turned into open collector outputs via bipolar transistors (MMBT2222AL) in order to drive the Shinsei driver. The inverted outputs of both TL3016 comparators are also routed into a logic NOR (TI SN74LVC1G86) to generate a dead zone control when the outputs of the two comparators are below their thresholds. The NOR's output disables the AD8180 multiplexer when neither clockwise nor counterclockwise signals are above threshold in order to prevent oscillations of the motor direction at low speeds.

The circuit board inside the MDM routes the incoming voltages to the Shinsei driver (24 V fused with 2.5 A), the attached encoder, and limit switches (5 V fused with 1 A). The circuit board also has five comparators for the encoder and limit switch signals that are received through three back panel connectors. The five comparators (TI LMH7220) receive the three differential encoder signals (A±, B±, index I±) and the single-ended forward and reverse limit switches, if present. The passive elements surrounding the comparator allow for both single-ended and differential inputs and are configured appropriately for each channel. A 2.5 V reference (not shown in the schematic of Fig. 23b) is used for both single ended and differential input configurations. The LVDS outputs of the comparators are then routed to the MCM via the front panel 15-channel cable.

3.3.5 Sensor interface module

The Sensor Interface Module shown in Figure 24a provides the front-end electronics for the tension and temperature sensors in the trolley drive system described in Section 3.2.1. A slightly modified version of the SIM serves as the interface for the emergency stops. Each SIM has an RJ-45 connector

on its front panel to provide power input, a differential analog output, and an LVDS comparator output. The back panel of the SIM has a 6-channel connector interface with the actual sensor.

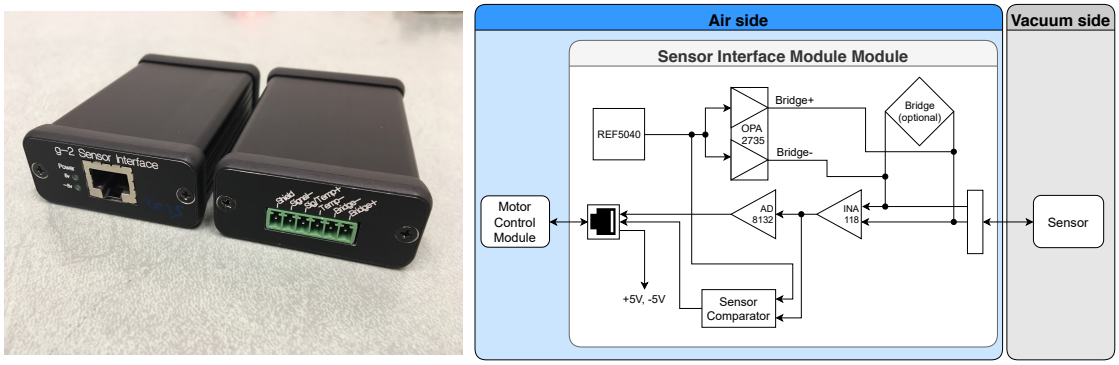

(a) (b)

Figure 24: (a) Front and back panels of the SIM and (b) a schematic of its main components.

The SIM input connects to a network of resistors that can either be configured for an external bridge (e.g. for the tension sensors) or to form an internal bridge to convert the value of the thermal resistors inside the temperature sensors to a voltage. The balanced power for the internal or external bridge comes from a precision 4.096 V reference (TI REF5040). Its reference voltage is then driven differentially by a dual op-amp (TI OPA2735) configured as a differential driver.

The sensor signal is low-pass filtered through a differential RC network. The signal is then amplified by an instrumentation amplifier (TI INA118). The gain for this amplifier is controlled by a single resistor and can be adjusted for each sensor type. The amplifier output is converted by a fully differential amplifier (AD AD8132). The differential ±2.5 V signal is terminated into 100 Ω and routed to the output connector to be sent to an analog channel of the MCM.

The output of the instrumentation amplifier (INA118) also connects to an LVDS comparator (TI LMH7220). This comparator provides an out-of-range hardware limit signal (Section 3.3.3) to form the basis for the All-Stop signal for all motors.

4The SIM module for the emergency stops only uses the comparator circuit while the signal amplification stage is not populated. The positive input of the LMH7220 comparator is set to 2.5 V and the inverting input is tied to the emergency stop switch. Under normal conditions, the switch is closed, which leads to a normally high output of the comparator logic. The emergency stops are also part of the All-Stop comparator logic in the MCM.

3.3.6 Software control and algorithms

During normal field scans, software safety checks guarantee the secure operation of the trolley. The basic motion sequences of the trolley and the garage system are managed by the Galil controller through Galil library functions and user-defined, application-specific control scripts interpreted by the system's microprocessor. Multiple subroutines can be executed in parallel and any relevant variables can be updated from the frontend computer.

The main scan routine reads the positions of the encoders, control voltages, limit switch statuses, and inputs from all analog channels. These values are sent to the frontend computer

with a Galil internal timestamp. The analog channels contain the readback from the tension sensors. If their values exceed a hardware-implemented threshold of ~50 N, all motion and running subroutines are aborted, and the motor drivers are disabled by turning off all +24 V power supplies. Additional protection was implemented through a software tension limit of ~40 N, which would stop the motion even before the hardware interlock takes action. A warning message is issued to the frontend computer for either of those tension trips.

For the trolley scanning motion, the drum that pulls the trolley ("driver") is rotating at a constant speed, while the other one ("follower") adjusts its speed to release the proper amount of cable and maintain the tension within a constant range on the driving cable. If the tension is initially above the limit, some cable is released by the driver. The movement is finished once the encoder from the drive has reached or exceeded the specified encoder position and the host system is informed. For the trolley insertion and extraction motions, the garage motor is maintained at a constant speed and the two cable drums will rotate synchronously to release (or wind) cable when the tension of the coax cable hits pre-defined high (or low) limits. The motion stops when either the garage motor encoder reaches a defined position or the limit switch at the end of the garage motion is engaged.

Run and slow control in the $g-2$ experiment are managed through MIDAS (see Sec. 2.6.3). A MIDAS frontend program on a Linux machine calls Galil library functions and user subroutines perform additional safety checks. The Galil readbacks are then merged to the MIDAS data stream every 0.5 s with a system timestamp, which is synchronized through the network time protocol (NTP) with all frontend machines.

A monitor thread decodes the messages from the Galil system, and these messages are stored through an online database (ODB) system to facilitate sanity and safety checks. For example, if an invalid Galil message is received, the monitor thread will abort motor motion. Likewise, if an emergency flag is found in the ODB, motor motion is halted. Control threads handle all motion commands from users and scripts. Motion is only allowed if the monitoring readback through the ODB verifies that all ring systems are in safe states. Such systems include two insertable beam monitors (fiber harp stations), retractable collimators, and the NMR calibration probe.

Besides calling the user-specified subroutines for the trolley motion, the frontend also provides an interface to individually move every motor. This is realized by directly calling the Galil library functions through the software. The motion of the NMR calibration probe is exclusively controlled in this way. The main motion commands for the field mapping systems are insertion and parking of the garage, clockwise (CW) and counterclockwise (CCW) trolley motion to the drive, and trolley motion back to the garage. The garage is always approached from ~4° downstream to prevent hysteresis affecting the position determination.

4 Performance

We performed dedicated measurements of various components to verify that the new trolley system met the requirements. Further analysis of the data acquired during the commissioning phase and the first data taking periods at Fermilab add to this verification. The results of various performance measurements will be reported in the following subsections. Section 4.1 provides details of the performance of individual NMR electronics components. Section 4.2 focuses on the upgrades of the mechanical drive and garage system along with its accompanying motion controller. The

last Section 4.3 presents the overall performance of the trolley's main functionality, the NMR measurements, and the precise mapping of the magnetic field in the muon storage region.

4.1 Performance of the NMR and barcode reader electronics

The NMR electronics (see Section 2) have undergone significant changes compared to the E821 system, and many components are entirely new. To verify their performances, the design incorporated various monitors for important parameters as described in Section 4.1.1. The crucial precision of the reference RF signal for the NMR mixer was tested through extensive phase noise measurements detailed in Section 4.1.2. The main concern for the data communication, which was time separated from the RF signal through TDM, was obtaining a sufficiently low bit error rate (see Section 4.1.3). The barcode reader was developed to meet the requirement for the azimuthal position determination as it directly impacts the field maps and calibration of the fixed NMR probes. Its performance is detailed in Section 4.1.4. Section 4.1.5 summarizes results on the reduction of the overall magnetic footprint of the trolley compared to the E821 system.

4.1.1 Status monitors for operation

Critical voltages in the trolley electronics include the incoming supply voltage and the analog sum of the regulated voltages on the NMR main board. The supply voltage depends on the current and resistance of the SCC, which slightly vary with the cable's tension. Throughout a typical field scan, the incoming voltage varies within ± 0.02 V. The regulated voltage averaged over a measurement cycle is the most relevant voltage for the NMR measurement. An example of the averaged voltage readout is shown in Fig. 25a. Its long-term variation is less than $\pm 5 \times 10^{-4}$ V. At short time scales of a measurement cycle, the regulated voltage drops by 7×10^{-3} V during the NMR measurement due to the sudden increase of the power consumption during the $\pi/2$ pulse and the FID signal amplification. This drop has a negligible effect on the extracted NMR frequency.

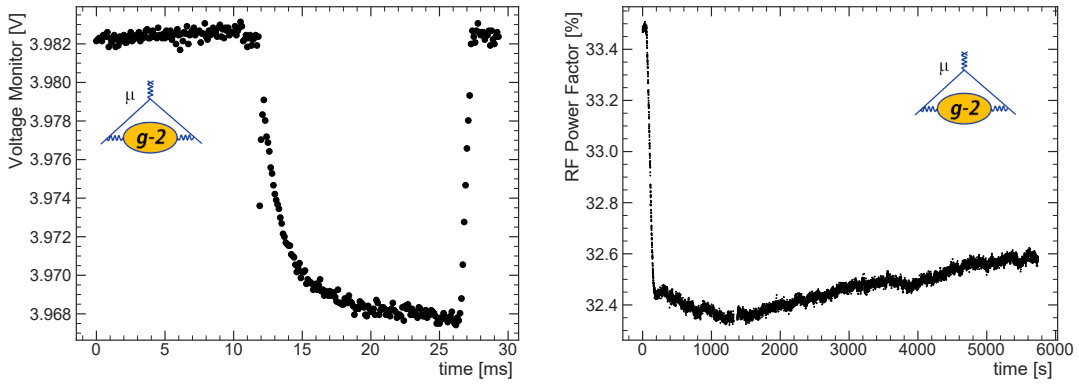

(a) (b)

Figure 25: a) Typical voltage readbacks of the linear superposition of the regulated voltages during an NMR readout cycle. b) Power factor of the RF signal received by the trolley electronics.

The power of the RF signal is monitored in the trolley via the ratio of the duty-cycle of two comparator outputs on the NMR main board. Fig. 25b shows this RF power factor from the time

when the garage starts inserting the trolley into the magnetic field. During the motion of the garage ($t < 240$ s), the magnetic field experienced by the trolley increases. When the field is close to 1.45 T, the RF oscillation is on resonance, and the impedance of the probe drops while the absorption in the probe becomes large. Therefore, the measured RF power drops abruptly during this process and then remains relatively stable. During the field scan, the RF power factor varies by 2×10^{-3}, a variation of less than 1 %, primarily resulting in a variation of the FID signal amplitude. However, the NMR frequency extraction algorithms are robust against this change in amplitude.

The temperature inside the trolley enclosure is monitored on the NMR main board and at the stem of the top-most probe. Temperature readbacks during a typical trolley measurement are shown in Fig. 26a. Because the heat is primarily generated in the electronics, the temperature measured on-board is always higher than at the probe. After 30 min from the beginning of a field scan, both temperatures increase linearly due to relatively stable power consumption. Throughout the entire field scan, the temperature measured at the probe stem increased by ~2 °C. This shifts the measured NMR frequency by a few ppb for the NMR probes used in the trolley. The pressure monitored on the main board also increases with the temperature during a field scan, as shown in Fig. 26b. Long-term pressure readbacks are stable, which indicates that there is no gas leak in the shell.

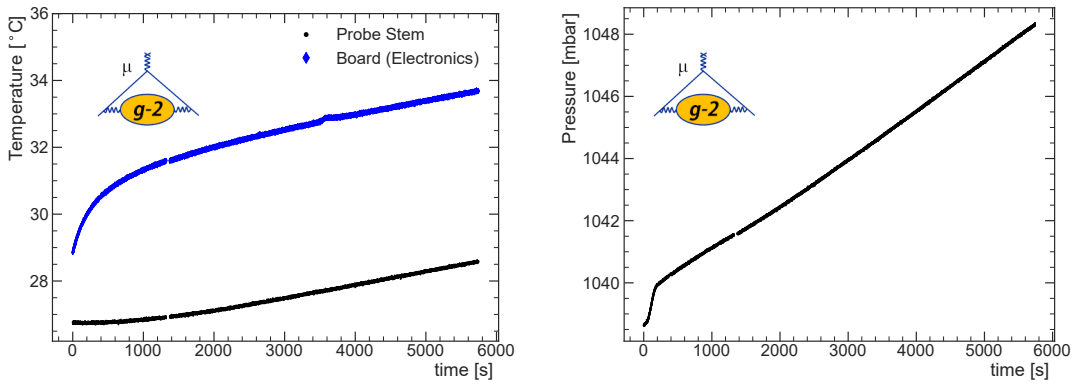

(a) (b)

Figure 26: a) The temperatures measured on the main board and at the stem of one NMR probe. b) The nitrogen gas pressure measured in the trolley enclosure.

4.1.2 Phase noise measurements

A central requirement for the NMR electronics described in Section 2.2 was the single-shot precision of better than 20 ppb for the NMR measurement. To meet this requirement, we derived the specification for the Allan deviation of the 61.74 MHz RF reference signal to be better than 1 ppb. The Allan deviation $A(\tau)$ for a bandwidth f_h can be derived from the phase noise $\mathcal{L}(f)$ via [13]:

$$A(\tau) = 2 \cdot \sqrt{\int_0^{f_h} 10^{\mathcal{L}(f)/10} \frac{\sin^4(\pi\tau f)}{\pi \nu_0 \tau} df},$$

where τ is the measurement period in the time domain, and ν_0 is the carrier frequency for the phase noise measurement. For the NMR measurements with the trolley system, typical FID signals are

on the order of a few ms long with the shortest signals in high gradient areas of about 1 ms or less. The low-pass filter in the systems determines the bandwidth to be f_h =100 kHz.

The phase noise measurements for various setups of the new NMR electronics were performed using a Keysight E5052B signal source analyzer. Figure 27 shows the phase noise measurements over the frequency range of 1 Hz to 10 MHz for different measurement setups. The green graph shows the simplest setup with the RF signal sent over the 50-m long coax cable alone. This configuration determined the achievable baseline for the phase noise with an Allan deviation of $A(1\,\text{ms}) = 0.3$ ppb. The addition of both coax drivers for the data communication alone shown in the blue graph increased the Allan deviation to $A(1\,\text{ms}) = 1.9$ ppb, already slightly above our goal. Adding just a clock signal for the data communication to the setup worsened it to $A(1\,\text{ms}) = 4.9$ ppb. Since the Allan deviation could further increase with the addition of the data communication, the design had to be changed by adding RF switches for the implementation of the TDM as described in Section 2.4.1. After the implementation of the TDM, the phase noise level for the crucial 61.74 MHz RF signal was restored to the baseline results of the green graph in Figure 27.

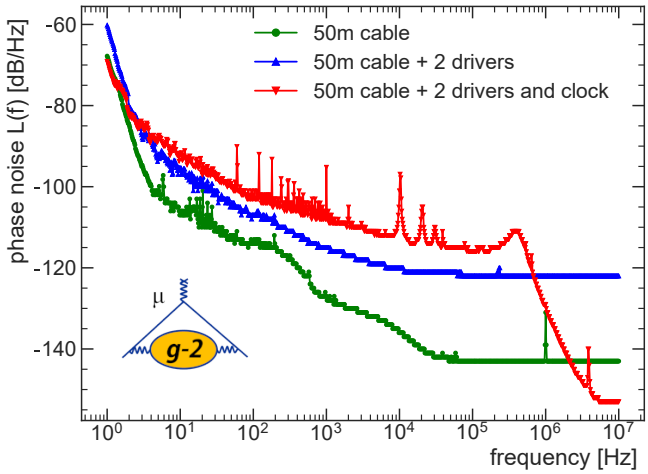

Figure 27: Phase noise measurements for different setups as explained in the text.

4.1.3 Data transmission and bit error rate

A critical test prior to finalizing the new SCC design was determining the achievable data transmission rate and the bit error ratio (BER). As explained in Section 2.4.1, we required a minimum of 200 kB/s for transmitting the data in parallel to the measurement. For the BER, the goal was less than 1 bit error per trolley run, corresponding to a maximal loss of one of the NMR measurement cycles. This level would not require the implementation of more sophisticated bit-error correction algorithms. As a full map of the azimuthal field with the trolley corresponds to $\sim 10^{10}$ bits, this translates into a maximum BER of 10^{-10}. Extensive bench tests with the prototype interface and trolley boards were performed. Over 11 days, more than $4 \cdot 10^{13}$ bits were transferred with a speed of 41.67 Mbps without a single error, corresponding to a BER limit of less than $7.5 \cdot 10^{-13}$ (90% CL). This is sufficiently low that no bit error should occur over the entire lifetime of the experiment. At the same time, the achieved data transmission rate of > 5 MB/s met the requirements.

4.1.4 Barcode readout and trolley position measurement

Typical digitized waveforms of the absolute and regular barcode patterns (see Sec. 2.5.7) are shown in Fig. 28. Algorithms were developed to find the extrema in the waveforms and the transition edges, and thus convert the analog waveforms into logic levels corresponding to the black and white barcode marks. The time spectrum of the converted logic levels are overlaid in Fig. 28 for both the regular and absolute barcode patterns. The latter are then converted into a unique binary number[10]. For each absolute barcode pattern, its binary code and its azimuthal position in the ring are recorded in a database. The positions of NMR readout events are determined through counting the regular mark offset from the nearby absolute patterns. By using one pair of absolute and regular barcode reader channels, azimuthal positions of ~93% of the ring can be determined. For the entire ring, the barcode contrast is always much higher than the electronic noise from the readers. The limiting factors are the printing quality of the barcode marks, the discontinuity of the barcode at the vacuum chamber transitions, and the non-uniform motion of the trolley after moving out from high-friction areas. Using both barcode reader groups, some of these issues can be overcome, and the percentage of the ring where positions can be determined through barcode analysis increases to ~98%. The position of the trolley can be determined with an accuracy better than 2 mm, and the repeatability of the position determination is better than 0.4 mm. The repeatability of the barcode position determination is crucial for comparison of field maps, as shown in Section. 4.3.2. For the remaining ~2% of the ring, the position is determined by interpolating the encoder readings.

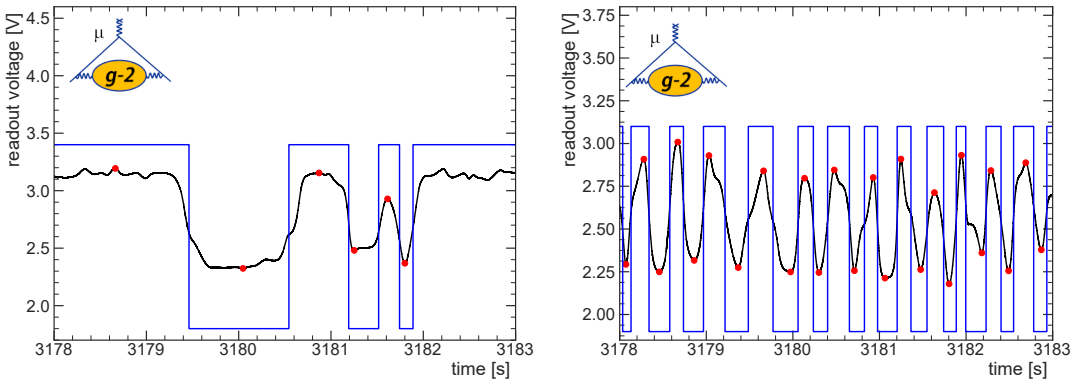

(a) (b)

Figure 28: Typical barcode patterns showing the raw digitized data (black), reconstructed maxima and minima (red dots) and derived binary pattern (blue) for a) one group of the absolute barcode channel and b) one regular barcode channel in the same region.

4.1.5 Magnetic footprint

During the implementation of the upgrades to the trolley system, special care was taken to use the least amount of magnetic materials. Every single electronics component was tested for its individual magnetic field distortion using test magnets at the University of Washington and Argonne National

[10]Some degeneracy exists in different parts of the ring.

Laboratory (ANL). The magnetic footprint of the final new trolley was carefully scanned along the trolley's long axis in the test solenoid at Argonne. The measuring NMR probe was placed at distances of $d = 7, 8, 9$, and 12 cm away from the center axis of the trolley. A full scan from end to end was performed for $d = 7$ cm as shown in the blue graph of Fig. 29. For other distances, only the parts with the largest magnetic footprint were scanned. The distance of the fixed probes to the trolley in the experiment corresponds to about $d = 9$ cm. However, due to the magnetic image effects in the nearby yoke iron above the fixed probes, the maximum effect of ~10 ppm in the experiment is larger than the measurements here. This is about factor of 2.5 smaller than in E821 [10]; meeting the requirement set for the new system.

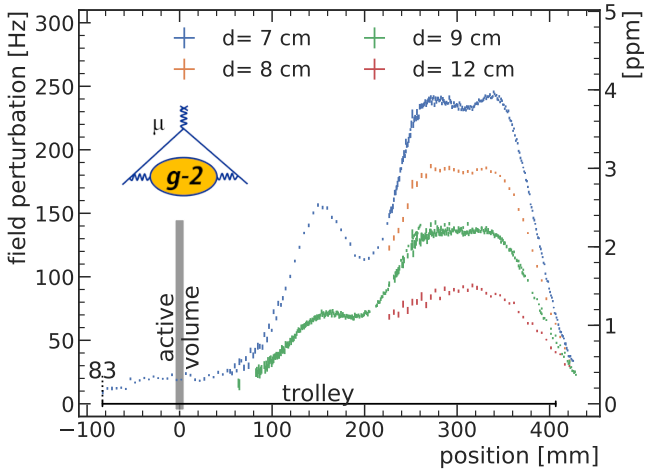

Figure 29: The magnetic footprint of the trolley measured along its long axis at various distances in the ANL test magnet. The measurement was obtained at the bottom side with respect to the trolley's orientation in the $g - 2$ experiment.

4.2 Performance of the mechanical and motion control systems

Since the commissioning of the Muon $g - 2$ experiment in 2016, more than 100 magnetic field scans have been performed with the trolley and its mechanical and control systems have proven to be reliable. During each field scan, various parameters monitor the performance and status of the system. The azimuthal position determined from the two drive motor encoders, cable tensions, and motor temperatures of a typical measurement are shown in Fig. 30. The control voltage is about 70% of the maximum range, and the motor speeds are about 120 RPM. The temperatures of the drive motors steadily increase during the operation but remain all below 38 °C. The motion control system maintains the cable pulling ("driving") motor at a constant velocity within 5% during the magnetic field scan. The "following" motor releases the cable to regulate the tension in the driving cable within the range from 10 N to 30 N and its velocity is adjusted within a ±15% range. When the trolley passes a rail discontinuity, the tension may increase above 30 N, resulting in isolated spikes in the tension curve shown in Fig. 30. A software tension trip threshold is set to 40 N.

Besides using the precise barcode reader (see Section 4.1.4) to determine the trolley's azimuthal position, it can also be approximated from the drive motor encoder readings via $\phi \approx k \frac{E_{nylon} - E_{coax}}{2}$,

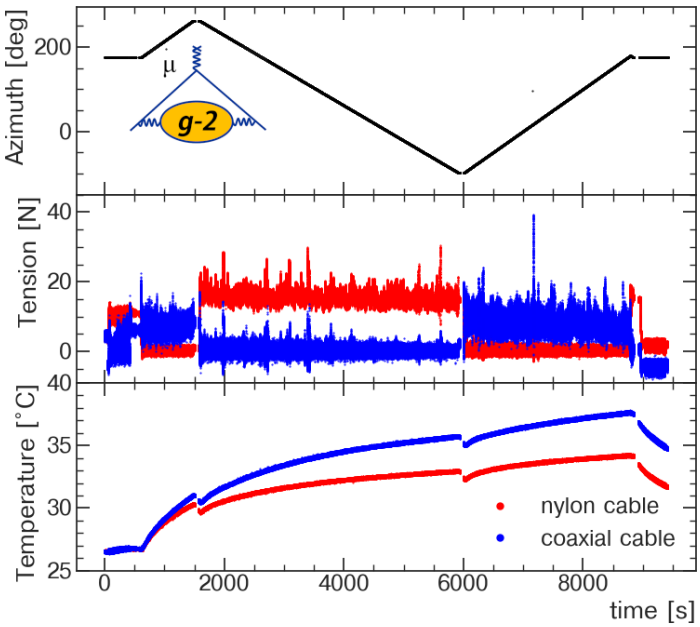

Figure 30: The trolley position determined by the drive motor encoders (top panel), tensions in the nylon and coaxial signal cable (middle panel), and temperatures of the motors (bottom panel) as a function of time during an entire field scan.

where E_{nylon} (E_{coax}) is the encoder reading of the motor that drives the nylon line (coaxial cable) and k is an experimentally determined constant. Because the cables are flexible, the position derived from the encoder readings does not accurately represent the trolley azimuthal position, particularly where the friction is high. The difference between the trolley position determined using the barcode analysis and the encoder readings is shown in Fig. 31. Throughout the entire motion, the two positions differ by up to ±0.15 degree (or 1.9 cm) mostly due to the encoders. Despite their lower accuracy, the encoders are used in the motion control and online position display because of the fast readback. The position information from the barcode is mainly used offline as its analysis is slow.

4.3 Performance of the magnetic field measurements via NMR

4.3.1 NMR signal quality and benchmark precision

The precision of the FID frequency extraction depends strongly on the length[11] of the FID and the uniformity of the local magnetic field in the probe's active volume. The benchmark precision of the trolley NMR system is measured in the region of the $g-2$ storage ring that is used for the trolley probe calibration. In this region, the magnetic field is shimmed to a higher level of uniformity, leading to typical FID lengths of ~10 ms. A typical, pedestal-subtracted, mixed-down FID waveform of the probe at the center of the trolley is shown in Fig. 32. The constant pedestal of the ADC is determined in measurement cycles without $\pi/2$ pulses. A full-length waveform is shown in Fig. 32a with the evolution of its envelope highlighted in blue. Focusing on the early

[11]The length of an FID signal is defined by the first time when the amplitude decays below $1/e$ of its maximum.

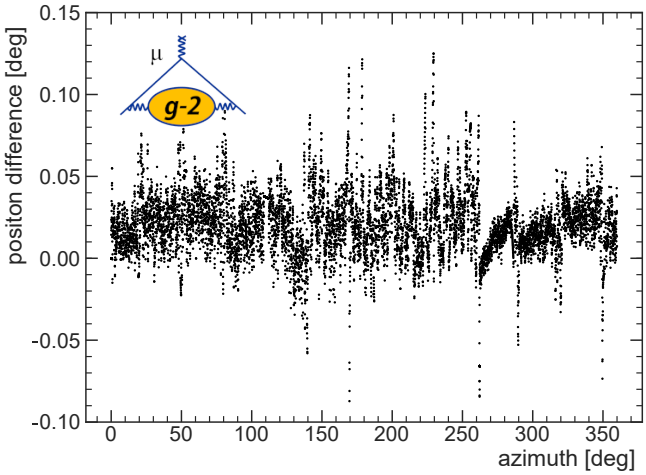

Figure 31: The difference of the trolley positions determined through the barcode analysis and the encoder readings. The trolley drive is located at ~262°.

part of the same FID in Fig. 32b shows start-up features stemming from the pre-amp along with a changing baseline after the strong $\pi/2$ pulse at 300 µs. The NMR pre-amp is turned on at 350 µs.

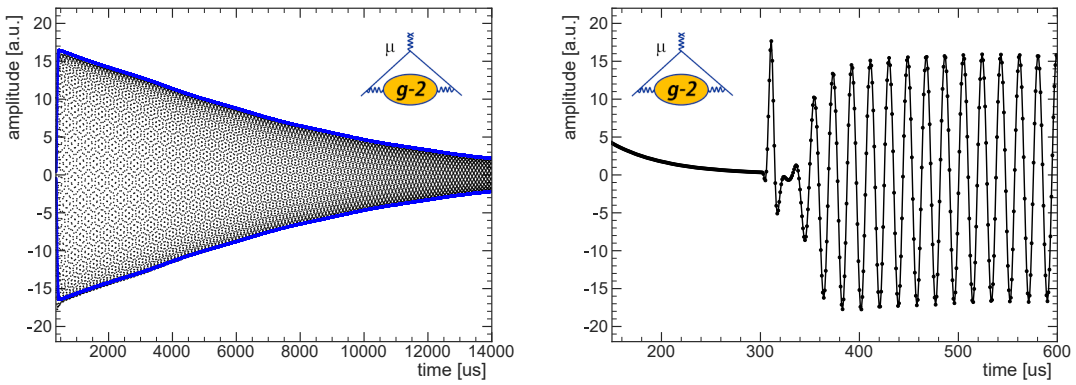

(a) (b)

Figure 32: (a) The digitized, pedestal-subtracted FID waveform from the center probe in the calibration region of the storage ring. The envelope shape is highlighted in blue. (a) Revealing signal distortions from the $\pi/2$ pulse and NMR pre-amp turn on in an early time window.

The average field observed by a probe can be determined through extracting the start-time derivative of the oscillation phase $d\Phi/dt(t = 0)$ [14], where $t = 0$ corresponds to the start time of the $\pi/2$ pulse. Therefore, the early section of the FID is crucial for the analysis. However, as shown in Fig. 32b, the baseline is non-constant before ~500 µs and the signal shape is distorted. The distortion reflects itself most prominently as an asymmetry of the amplitude of the maxima and minima of the baseline-subtracted FID signal. The effects from both a slowly varying baseline and the signal asymmetry were extensively studied [15] both with data and simulated FID signals.

These effects are mitigated using the FID frequency extraction method we developed, and for a 10 ms long FID, the associated systematic uncertainty is less than 1 ppb.

Noise in the system results in a statistical uncertainty of the extracted frequency, which is the resolution of a single shot. The noise in the NMR waveform is measured by analyzing full FID signals that were taken in a magnetic field outside of the dynamic range of the system. This setup includes all the electronic noise that is introduced in the system. The root mean square (RMS) noise is ~0.3% of the maximum amplitude of typical FIDs, and the noise has a frequency cut-off at ~90 kHz due to the low-pass filters in the electronic system. The statistical uncertainty caused by such a noise is less than 0.03 Hz for a 10 ms long FID. However, random fluctuations of the magnetic field, either intrinsic to the field itself or introduced by the trolley, also matter for the magnetic field measurement. Therefore, as a benchmark for the probes' precisions the RMS of 24 events in the calibration region were used as shown in Fig. 33. The precision is below 7 ppb (0.43 Hz) for all trolley probes, meeting our single shot precision requirement of less than 20 ppb.

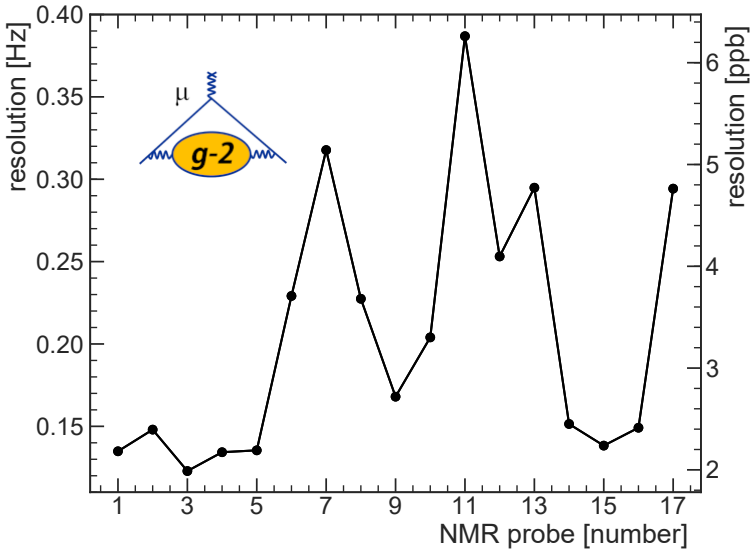

Figure 33: Precisions for all trolley probes evaluated from data taken in the calibration region.

4.3.2 Magnetic field maps

A magnetic field scan consists of roughly 9000 measurements per probe and direction, which corresponds to an azimuthal resolution of about 0.04°. Subsequent measurements from the 17 trolley probes are combined to one azimuthal slice which is fitted with a 2D-multipole expansion [2]. These slices are then combined to form a full three-dimensional map of the fitted multipoles. A typical, azimuthally averaged transverse field distribution and the variation of the dipole from the average are shown in Figures 34a and 34b, respectively.

In regions near the boundaries of the magnet iron yokes, the field gradient can be as high as 0.75 ppm/mm. In such regions, the position determination repeatability is particularly important for studying the field drift between two scans. The frequency seen by the center probe during

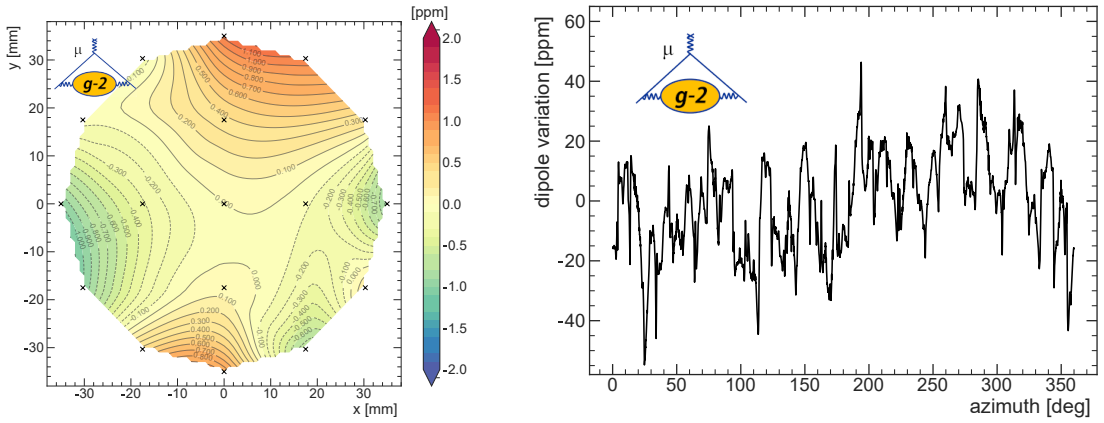

(a) (b)

Figure 34: Representative magnetic field distributions taken during Run-1 in 2018 showing (a) the azimuthally averaged, transverse field distribution and (b) the dipole variation versus azimuth.

a clockwise (CW) and a counter-clockwise (CCW) scan are compared using the barcode reader information or the motor encoders in Figures 35a and 35b, respectively. The CW and CCW scans are typically separated by only 1 h. Therefore, field drifts at a scale of ∼1 kHz (16 ppm), as seen in Fig. 35b, are not expected. This illustrates the significant improvement stemming from the barcode information for the precise evaluation of field maps.

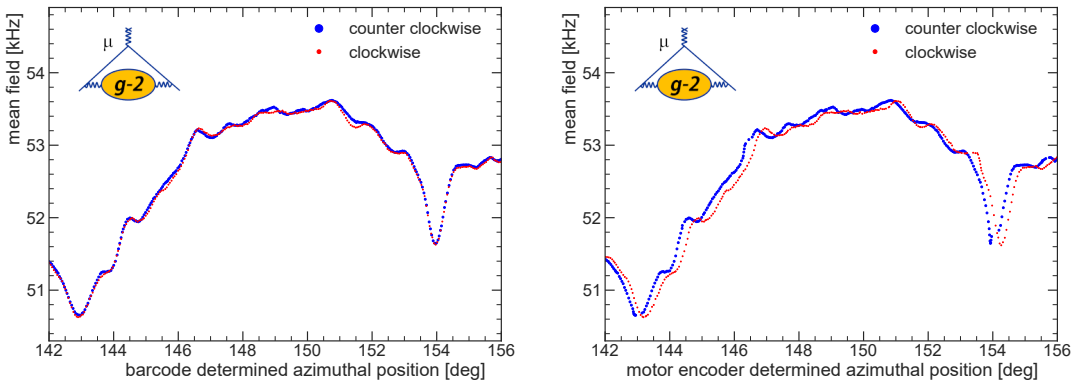

(a) (b)

Figure 35: The magnetic field at the center trolley probe in counter-clockwise and clockwise direction scans in the same azimuthal region using (a) the barcode position determination and (b) the motor encoder readings.

Magnetic field inhomogeneities reduce the FID length. Since the average field around the ring is less homogeneous than in the optimized calibration region, the frequency extraction precision is worse than the benchmark presented in Section. 4.3.1. Approximately, the FID length scales inversely proportional to the field gradient in the azimuthal direction $\frac{\partial B}{\partial \Phi}$, and the frequency precision

of an FID scales approximately to $1/T \ln(T)$ where T is the FID length. According to studies performed with simulated FIDs, the precision of the frequency extraction for FIDs measured in a field gradient $\frac{\partial B}{\partial \Phi} = 60\,\text{Hz/mm}$ is about 25 Hz. However, more than 80% of the FIDs have precisions better than 2 Hz (32 ppb). On the other hand, the magnetic field value relevant to the muon spin precession is the averaged magnetic field in the beam storage region. Due to the large number of measurements around the ring, the uncertainty related to the frequency extraction is reduced by a factor of ~100 from this typical single-shot precision. According to the magnetic field gradients measured in field scans and the FID frequency extraction precision studies, the statistical uncertainty (precision) of the azimuthally averaged field of each probe is less than 0.06 Hz (1 ppb). Due to dynamic effects generated by motion induced Eddy currents in the conductive materials of the trolley, the observed probe precision during the trolley movement is more than one order of magnitude worse than in this static case. Studies are ongoing to determine the final systematic uncertainty of the field maps relevant to the determination of ω_p and with it a_μ. The results of these will be reported in future publications of the Muon $g-2$ collaboration.

5 Conclusions

The existing NMR field mapping system from the BNL E821 experiment was successfully refurbished and upgraded at Argonne National Laboratory with help from other Muon $g-2$ collaborating institutions. The NMR electronics were significantly upgraded with modern components to replace the obsolete trolley micro-controller and to allow for the addition of full NMR signal digitization. A new time-division multiplexing (TDM) scheme separates the precise RF reference signal from the data communication in order to achieve a benchmark precision for the NMR measurement of better than 20 ppb. A new barcode reader has improved the azimuthal position determination, which is crucial for the precise field mapping in high-gradient regions of the storage ring. The NMR electronics components located outside of the vacuum chambers were completely replaced with the new interface to facilitate the new TDM scheme implemented in the trolley.

The new motion controller for the mechanical drive and garage systems replaced the obsolete controller from E821. The new system is centered around a Galil motion controller and integrates both the control of the piezo-electric Shinsei motors and readbacks from sensors and limit switches.

The new trolley electronics, the trolley interface, and the new motion control system have been operated very reliably during the first data taking periods of the Muon $g-2$ experiment. Extensive measurements and analyses of the acquired data show that the system meets the original requirements defined prior to the design of the new system. Ongoing analyses and studies will further help to determine the final precision achieved for the determination of ω_p and a_μ.

Acknowledgments

We would like to thank our colleagues from ANL for their help during the design phase: Frank Skrzecz, Ken Wood, and Allen Zhao for their valuable input on the mechanical upgrades; Gary Drake for his supervision and advice on the electronics engineering; Carol Adams, Tim Cundiff, and Bill Haberichter for the assembly of electronics components. We thank Peter von Walter for his time at ANL to transfer knowledge from the former trolley system to our group. Many $g-2$

collaborators helped through discussions or with information that was crucial to the implementation of the upgrades. We thank Erik Swanson, Rachel Osofsky, and Martin Fertl for the NMR probes. We appreciate the Department of Defense for transferring a 4 T test solenoid that was very useful for many measurements. This research was supported by the U.S. Department of Energy, Office of Science, High Energy Physics under contracts DE-AC02-06CH11357 (Argonne National Laboratory), DE-FG02-88ER40415 (University of Massachusetts), and by Fermi National Accelerator Laboratory (Fermilab), a US DOE, HEP User Facility. Fermilab is managed by Fermi Research Alliance, LLC (FRA), acting under Contract No. DE-AC02-07CH11359.

References

[1] Muon g-2 collaboration, J. Grange et al., *Muon (g-2) Technical Design Report*, 1501.06858.

[2] Muon g-2 collaboration, G. W. Bennett et al., *Final Report of the Muon E821 Anomalous Magnetic Moment Measurement at BNL*, *Phys. Rev.* **D73** (2006) 072003, [hep-ex/0602035].

[3] F. Jegerlehner, *Muon g – 2 theory: The hadronic part*, *EPJ Web Conf.* **166** (2018) 00022, [1705.00263].

[4] M. Davier, A. Hoecker, B. Malaescu and Z. Zhang, *Reevaluation of the hadronic vacuum polarisation contributions to the Standard Model predictions of the muon $g-2$ and $\alpha(m_Z^2)$ using newest hadronic cross-section data*, *Eur. Phys. J.* **C77** (2017) 827, [1706.09436].

[5] A. Keshavarzi, D. Nomura and T. Teubner, *Muon $g-2$ and $\alpha(M_Z^2)$: a new data-based analysis*, *Phys. Rev.* **D97** (2018) 114025, [1802.02995].

[6] M. Davier, A. Hoecker, B. Malaescu and Z. Zhang, *A new evaluation of the hadronic vacuum polarisation contributions to the muon anomalous magnetic moment and to $\alpha(m_Z^2)$*, *Submitted to EPJ-C* (2019) , [1908.00921].

[7] A. Yamamoto et al., *The superconducting inflector for the BNL g-2 experiment*, *Nucl. Instrum. Meth.* **A491** (2002) 23–40.

[8] A. T. Fienberg et al., *Studies of an array of PbF_2 Cherenkov crystals with large-area SiPM readout*, *Nucl. Instrum. Meth.* **A783** (2015) 12–21, [1412.5525].

[9] A. Großmann, *Magnetic Field Determination in a Superferric Storage Ring for a Precise Measurement of the Muon Magnetic Anomaly*. PhD thesis, Ruprecht-Karls-Universität Heidelberg, Germany, 1998.

[10] H. Deng, *Precise Measurement of the Positive Muon Anomalous Magnetic Moment*. PhD thesis, Yale University, New Haven, CT, USA, 2002.

[11] R. Prigl, U. Haeberlen, K. Jungmann, G. zu Putlitz and P. von Walter, *A high precision magnetometer based on pulsed NMR*, *Nucl. Instrum. Meth.* **A374** (1996) 118–126.

[12] D. Flay and D. Kawall, *The High-Precision Calibration NMR Magnetometer for the Muon $g-2$ Experiment at Fermilab*, *in preparation* (2020) .

[13] W. Riley, *Handbook of frequency stability analysis*, *NIST* **1065** (01, 2007) 1–123.

[14] B. Cowan, *Asymmetric NMR lineshapes and precision magnetometry*, *Measurement Science and Technology* **7** (1996) 690–695.

[15] R. Hong et al., *Systematic and Statistical Uncertainties of the Hilbert-Transform Based High-precision FID Frequency Extraction Method*, *in preparation* (2020) .